Electrochemical reduction of CO_2 to CO in a flow-through electrolyser

Niels Goos
4232216

May 2020

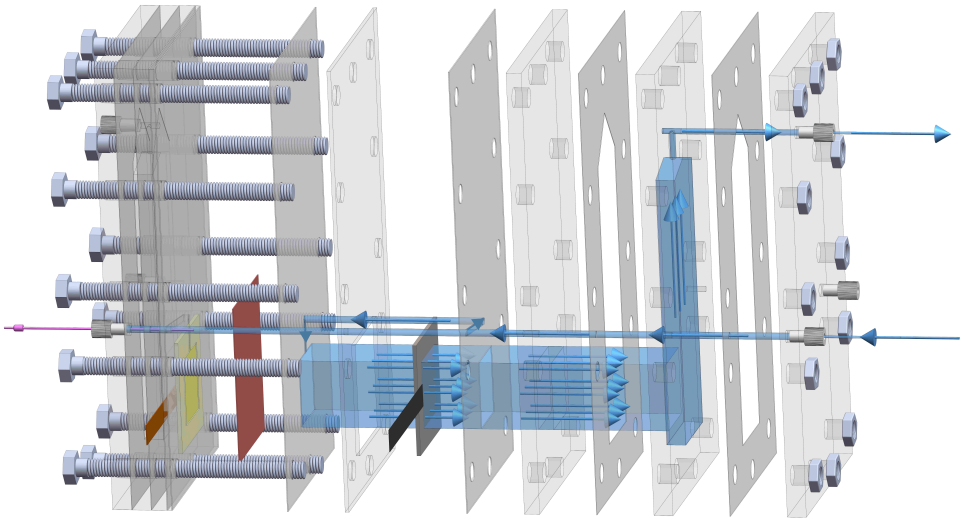

Abstract

Electrochemical reduction of the CO_2 into the chemically valuable CO at an industrial scale is a promising way to reverse the worrying rise of CO_2 levels in the atmosphere. Profitable operation at an industrial scale requires high CO partial current densities, producing a CO-rich output, while keeping the energy consumption and the price of the electrolyser low. Conventional CO_2 reduction (CO_2R) to CO electrolysers suffer from the competing hydrogen evolution (HEV) reaction and mass transport limitations. Therefore, they can produce a maximum CO partial current densities of 20 mA cm^{-2}. The current densities can be increased by working at higher pressures or using gas diffusion electrodes, but to date, both require high energy inputs.

Therefore, we investigated the potential of using a flow-through electrolyser (FTE) to produce CO partial current densities exceeding the 20 mA cm^{-2}, while keeping the potential attractive. Porous flow-through electrodes can overcome mass transport limitations by their large reactive surface area and their ability to decrease the diffusion boundary layer thickness. To obtain suitable porous electrodes, we electrodeposited Ag on microporous Ti substrates. We used an aqueous CO_2-saturated $KHCO_3$ solution, as a well-proven electrolyte for CO_2R to CO on a Ag catalyst.

Our FTE was capable of overcoming the mass transport limitations. In a one-off test, it produced a CO partial current density of 100 mA cm^{-2}, at a Faradaic efficiency (FE) of 55 %. We could reproduce CO partial current densities of 60 mA cm^{-2} at a FE of 25 % in a 0.05 M $KHCO_3$ solution. We experienced a decrease in activity towards CO when using more concentrated electrolytes.

However, high cell potentials of more than 5 V, were required to exceed CO partial current densities of 20 mA cm^{-2}. The required high potentials can be ascribed to ohmic losses and low selectivities towards CO. We believe that the insufficient deposition of the Ag on the microporous Ti electrode was the main reason for the low selectivity.

Implementing the improvements, that are mentioned in the report, could contribute to make the FTE a promising candidate to reduce CO_2 to CO at an industrial scale effectively.

Contents

Nomenclature

Physics Constants

F	Faraday Constant	9.6485×10^4 C mol^{-1}
R	Ideal gas constant	8.31446 J K^{-1} mol^{-1}

Variables

$\boldsymbol{J}_j$	Flux of component j	mol m^{-2} s^{-1}
Δp	Pressure drop over the thickness of the electrode	Pa
δ_{D}	Diffusion boundary layer thickness	m
Δ_{gap}	Pressure drop over the length of the gap	Pa
ϵ	Void fraction	1
ϵ_{Ag}	Fraction of Ag particles in the electrode	1
ϵ_{gas}	Gas fraction	1
η	Overpotential	V
η_{act}	Activation overpotential	V
κ	Ionic conductivity	S m^{-1}
κ_{eff}	Effective conductivity	S m^{-1}
μ	Dynamic viscosity	Pa s
ρ	Volumetric mass density	kg m^{-3}
ρ_{el}	Apparent volumetric mass density of the porous electrode	kg m^{-3}
ρ_{Ti}	Volumetric mass density of Ti	kg m^{-3}
σ	Electrical conductivity	S m^{-1}
a	Specific surface area	m^2 m^{-3} = m^{-1}
A_{i}	Surface of a single particle	m^{-2}
a_{sphere}	Specific surface area of a sphere	m^{-1}
A_{in}	Internal surface area	m^2
$A_{\perp}$	Frontal surface area	m^2
b	Tafel slope	V
C_{Bulk}	Bulk concentration	mol m^{-3}
C_j	Molar concentration of species j	mol m^{-3}
D_j	Diffusion coefficient of compound j	m^2 s^{-1}
d_p	Diameter of sintered particles in electrode	m
E	Half cell potential	V
$E_{0'}$	Formal potential	V
h	Height of the channel between the electrode and the BPM	m
i	Current density	A m^{-2}
i_{m}	Migration current density	A m^{-2}

i_{con}	Convection limited current density	A m^{-2}
$i_{\mathrm{in,dif}}$	Diffusion limited current per internal surface area	A m^{-2}
i_{in}	Current density per internal surface area	A m^{-2}
i_{o}	Exchange current density	A m^{-2}
L	Thickness of the electrode	m
M	Molar mass	kg mol^{-1}
n	Stoichiometric coefficient	1
p	Pressure	Pa
P_{pump}	Pump power	W
$Q_{\mathrm{electrolyte}}$	Volumetric flux of the electrolyte	m^3 s^{-2}
Q_{gas}	Volumetric flux of the gas	m^3 s^{-2}
t_{depo}	Deposition time	s
u	Electrical mobility of the ion	m^2 s^{-1} V^{-1}
$V_{\mathrm{electrolyte}}$	Volume of the electrolyte in the electrode	m^3
V_{gas}	Volume of the gas in the electrode	m^3
v_{pore}	Average velocity in the pores	m s^{-1}
V_i	Volume of an individual particle i	m^{-3}
v_s	Superficial flow velocity	m s^{-1}
V_{el}	Apparent electrode volume	m^{-3}
V_{pore}	Reachable volume of the pores	m^{-3}
w	Width of the flow channel of the FTE	m
x	Horizontal coordinate over the thickness of the electrode	m
z	Charge number	1
T	Temperature	K

Chemical Compounds

AgCl	Silver chloride
$AgNO_3$	Silver nitrate
CO_2	Carbon dioxide
$CO_3{}^{2-}$	Carbonate
CO	Carbon monoxide
H_2O	Water
$HCO_3{}^-$	Bicarbonate
$KHCO_3$	Potassium bicarbonate
KOH	Potassium hydroxide
$LiClO_4$	Lithium perchlorate
Ag	Silver

Au	Gold
Ni	Nickel
Ti	Titanium
Zn	Zinc

Acronyms

BPM	Bipolar membrane
EDS	Energy-dispersive X-ray spectroscopy
FE	Faradaic efficiency
FTE	Flow-through electrolyser
GC	Gas chromatograph
GLS	Gas-liquid separator
HEV	Hydrogen evolution
HPLC	High performance liquid chromatography
ICP-OES	Inductively coupled plasma optical emission spectroscopy
SEM	Scanning electron microscope
CO_2R	Carbon dioxide reduction
SHE	Standard hydrogen electrode

1 Introduction

The CO_2 concentration in the atmosphere of the earth is rising at a worrying speed, due to human activities since the industrial revolution (1800 AD). Before that, concentrations were rising at a rate of 30 ppm per 1000 years [17], compared to a rise of 60 ppm over the last 30 years, reaching a concentration of 414 ppm today (April 2020) [16]. These rising concentrations of CO_2 contribute to global warming, caused by the greenhouse effect [31]. One pathway to promote a decrease in CO_2 levels is to transform CO_2 into value-added, carbon-containing products, to re-use the emitted carbon. Electrochemical reduction of CO_2 into valuable carbon-containing substances is a promising technique to mitigate the levels of greenhouse gasses, by using renewable energy [20].

Converting CO_2 into a CO-rich gas stream is of much interest for industry [65], since CO can be used as an intermediate substance for producing chemical products, such as methanol, ammonia or synthetic hydrocarbon fuels via the Fischer-Tropsch process [75]. The reduction of CO_2 to CO suffers from the competitive hydrogen evolution (HEV) reaction and mass transport limitations. These limit the current density to 20 mA cm^{-2}, when using conventional electrolysers [24]. They use planar electrodes, operate at ambient pressure, room temperature, and without flow. The low solubility of CO_2 in aqueous electrolytes in combination with the thick concentration boundary layer, limits the concentration gradient. Thereby, limiting the transport of CO_2 to the electroactive surface of the electrodes by diffusion. In contrast, commercial electrolysers can produce more than 200 mA cm^{-2} [55]. Research shows increased current densities when operating at elevated pressures or when using gas-diffusion electrodes (GDE). Lamaison et al. [33] produced a CO partial current density of 286 mA cm^{-2}, at a pressure of 9.5 bar. Increased current densities can be addressed to higher CO_2 solubilities at elevated pressures. Tornow et al. [60] obtained CO partial current densities of 95 mA cm^{-2}, at a cathode potential of -1.8 V, room temperature and ambient pressure in GDEs. Nevertheless, in electrolysers that use GDEs, the CO_2 source stream mixes with the product stream at the electrode. This requires an energy-intensive separation step to obtain a CO-rich output [74]. Creating elevated pressures requires high energy input and put higher mechanical demands on the system. Rather, we use a more elegant solution to produce high current densities, while minimising energy losses in the whole system.

An FTE could be used to overcome mass transport limitations. The flow-through design was used to decrease the diffusion boundary layer thickness and increase the reactive surface area. Thereby, they allow for higher current densities, without requiring elevated pressures or having CO_2 streams in the electrode. Bumroongsakulsawat and Kelsall [9] successfully used an FTE to overcome mass transport limited currents of CO_2R, but produced formate as the major product, since they used a Sn catalyst.

Research into the use of FTEs for CO_2R to CO in aqueous electrolytes and suitable porous 3D electrodes is lacking, to our knowledge. This research, therefore includes the production of a porous 3D electrode by electrodeposition of a Ag catalyst on a porous Ti substrate. Ag is known to be a suitable catalyst for CO_2R to CO. We used an aqueous $KHCO_3$ electrolyte, since its use for CO_2R to CO is well studied. The input of the system will be a gas stream with a high concentration of CO_2, representing an exhaust gas stream from industry. We researched the potential of using FTEs for CO_2R to CO at high CO partial current densities, while keeping the overpotential attractive, suppress HEV, and generate a CO-rich gas output.

In this research, we explained the theory to describe the FTE. Next to that, we have quantified some parameters in the FTE, by modelling. Subsequently, we present qualitative and quantitative results of the in situ measurements, defining the performance of the FTE. In the end, we formed a conclusion about the potential of using an FTE for CO_2R to CO.

2 Theory

In this section, we explained the theory that we used to describe our setup. The mathematical expression that helped us to define our system quantitatively are included. The simplifications and assumptions that were made are discussed. We required certain conditions to ensure an efficiently operating setup.

We first discuss the FTE and porous electrodes. Then we treat the electrochemical reduction of CO_2 to CO on a Ag catalyst, in a $KHCO_3$ solution. At last, we discuss the electrodeposition of Ag on porous Ti. Be aware that we discuss the concepts briefly. A thorough understanding of the used theory requires further reading. For a detailed explanation of the electrochemistry we refer to Bard and Faulkner [8].

2.1 Flow-through electrolyser

A key element in the FTE configuration is the porous electrode. The porous electrode enables the transport of electrons through the electroconductive material. Simultaneously the pores create space for the electrolyte to flow through and transport ions. All the pores enhance the internal surface area of the electrode, also known as is the electrolyte-electrode interface. In the FTE used in this research (see fig. 1), two flat porous electrodes are clamped parallel to each other, with a gap in between. The electrolyte is supplied via the gap and pumped through the electrodes. The gases, formed at the electrodes, are advected along with the electrolyte flow, away from the counter electrode. Separation of the oxidation and reduction product gases is made possible by the flow. This would not be possible in different flow-through or flow-by electrolysers where the flows of electrolyte are in other directions [61]. In flow batteries flow-through normally indicated a flow of electrolyte normal to the ion flow, which is less effective in advecting away the products [5, 4, 76].

Previous studies [6, 19, 29] show a similar configuration for the production of hydrogen. They claimed the to obtain benefits from using a flow-through design (i) the absence of a membrane, (ii) simplified overall design that results in a reduction of capital cost and lower maintenance, and (iii) simplified but effective gas separation. The reduction of CO_2 to CO has different characteristics compared to HEV. These, later explained, different characteristics led us to the use of a bipolar membrane (BPM) in between the electrodes, creating a separate stream for the catholyte and anolyte.

Relevant dimensions of the FTE can be found in fig. 1. For this work, we used electrodes constructed of sintered Ti particles. We have simplified the particles as spheres, to be able to describe the electrode quantitatively. We will now discuss void fraction, specific surface area, pressure drops, current densities and gas formation.

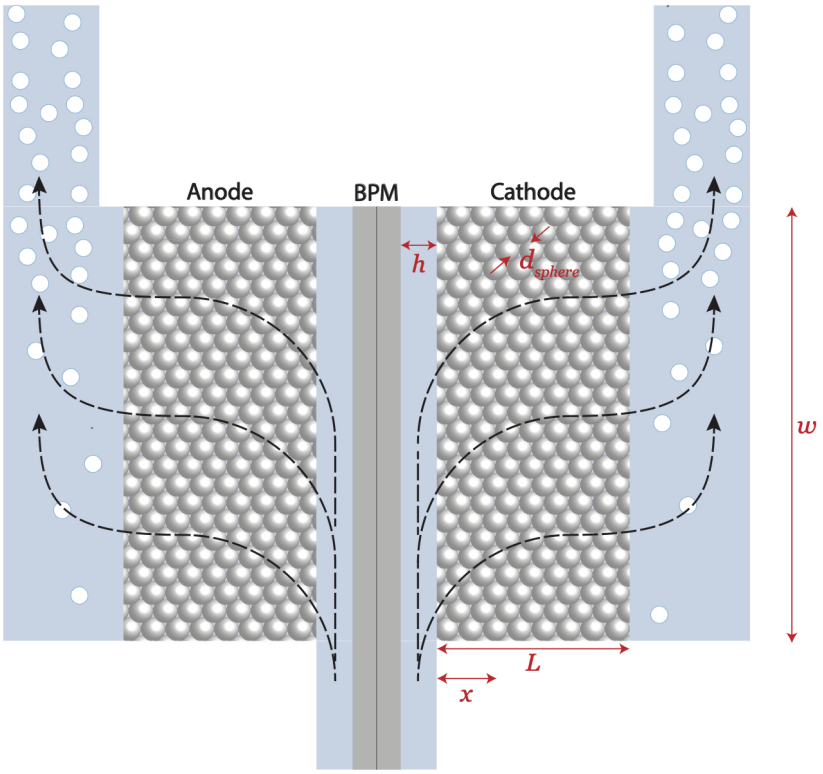

Figure 1: Schematic vertical cross-section view of the FTE, parallel to the flow direction. The catholyte and anolyte are separated by a BPM. Shown in black is the flow direction of the electrolytes. The white circles represent the gaseous products. The h is the gap width of the channel before electrodes, d_p is the particle diameter, w is the width and height of the electrode, L is the thickness of the electrodes, and x is the coordinate, where x=0 is the front side of the electrode, closes to the counter electrode.

2.1.1 Void fraction

The void fraction, or porosity, ϵ, quantifies the fraction of accessible space that the electrolyte can reach. The void fraction is defined as [71]

$$\epsilon \equiv \frac{V_{\text{pore}}}{V_{\text{el}}}, \tag{1}$$

which is expressed in terms of reachable pore volume V_{pore} and apparent electrode volume V_{el}. The latter is defined as the total volume that is occupied by the electrode, i.e. the combined volume of the Ti particles and the pores. When considering the individual volume of the particles V_i, we read

$$\epsilon = 1 - \frac{\sum_i V_i}{V_{\text{el}}}. \tag{2}$$

We calculated the void fraction of our electrodes using the measured apparent density of the porous electrode ρ_{el}, and the density of Ti ρ_{Ti}, as

$$\epsilon = 1 - \frac{\rho_{\text{el}}}{\rho_{\text{Ti}}}. \tag{3}$$

Hereby, we assumed that all the voids are accessible by the electrolyte and that the particles are made of pure Ti. This makes the ratio of the last parts of eqs. (2) and (3) identical.

2.1.2 Specific surface area

We define the specific surface area a, as the amount of internal surface area A_{in}, per apparent electrode volume V_{el} [10]. The specific surface area can be expressed as

$$a \equiv \frac{A_{\text{in}}}{V_{\text{el}}} = (1-\epsilon)\frac{\sum_i A_i}{\sum_i V_i}, \tag{4}$$

where A_i is the surface of a single particle. We simplified the particles as equally sized spheres. Therefore a can be expressed in terms of the diameter of a sphere d_{sphere}, such that

$$a \approx (1-\epsilon)a_{\text{sphere}} = (1-\epsilon)\frac{A_{\text{sphere}}}{V_{\text{sphere}}} = (1-\epsilon)\frac{6}{d_{\text{sphere}}}, \tag{5}$$

where a_{sphere}, A_{sphere}, and V_{sphere} are the specific surface area, the surface area, and the volume of the sphere, respectively.

2.1.3 Pressure drop

The pressure drop over the electrode can be calculated with the Ergun equation [14], which reads

$$\Delta p \equiv \frac{150\mu L}{d_{\text{sphere}}^2}\frac{(1-\epsilon)^2}{\epsilon^3}v_s + \frac{175\rho L}{d_{\text{sphere}}}\frac{1-\epsilon}{\epsilon^3}v_s^2. \tag{6}$$

For the dynamic viscosity μ, and the density ρ, of the electrolyte, we assumed the dynamic viscosity and density of the electrolyte to be equal to those of water. The length L, is the thickness of the electrode and v_s is the superficial velocity through the electrode. The effect of the production of gas bubbles in the electrode was not considered. The calculated pressure drop can be used to calculate the power consumed by the pump [38],

$$P_{\text{pump}} = \frac{\frac{\Delta p}{L}A_\perp v_s}{\eta_{\text{eff,pump}}}, \tag{7}$$

where $A_\perp$ is the frontal surface area of the electrode and $\eta_{\text{eff,pump}}$ is the efficiency of the pump, which can be can be obtained from pump curves [72]. The pump power can be compared with the power loss due to overpotentials. Furthermore, the pressure drop over the electrode should be much higher than the pressure drop over the gap,

$$\Delta p \gg \Delta p_{\text{gap}}, \tag{8}$$

such that the electrolyte will flow uniformly through the electrode. The pressure drop over the gap can be defined by the Hagen-Poiseuille equation for a flow between two planes [13],

$$\Delta p_{\text{gap}} = \int_0^w 12\mu\frac{Q(z)}{wh^3}dz = \frac{6\mu Q}{h^3}, \tag{9}$$

where h is the width of the gap, w is the height and width of the electrode and therefore also the height of the gap. The volume flux of the electrolyte $Q_{\text{electrolyte}}$, should be dependent on the z-coordinate, since the volume flux decreases in the z direction. This is because the flow passes through the electrode along the path of the gap. We simplified this as if all the electrolyte would flow through half of the gap height, so the pressure drop becomes equal to the last part of eq. (9).

2.1.4 Current density

The movement of electrons in the electrode and ions in the electrolyte causes the movement of charge. The charge transfer between these two takes place at the electrode-electrolyte interface. Here, we describe the relation between the migration current density i_{m}, movement of ions, and the Faradaic current density over the internal surface area i_{in}, which represents the charge transfer from the electronic current to ionic current. The internal current density i_{in}, in our cathode is non-homogeneously distributed over the electrode thickness and is therefore a function of the x-coordinate (see section 2.2.5). All the $i_{\text{in}}(x)$ has to be transported between the electrode interface and the opposing electrode. Therefore, the i_{m} accumulates towards the opposing electrode an can thus be expressed as the integration from L to x,

$$i_{\mathrm{m}}(x) = \int_{L}^{x} i_{\mathrm{in}}(x) a \, dx, \tag{10}$$

or can be rewritten as

$$i_{\mathrm{in}}(x) = -\frac{1}{a} \frac{\partial i_{\mathrm{m}}(x)}{\partial x}, \tag{11}$$

2.1.5 Gas formation

Gaseous products are produced within the porous electrodes. As the gaseous products exceed the saturation concentration, bubbles are formed. The gas bubble fraction in the electrolyte decreases the effective conductivity. The bubbles also block and inactivate the active surface area. Both effects drive the overpotential and lead to a redistribution of the current [27]. A sufficient flow of electrolyte can diminish these effects, as the bubbles will be advected by the electrolyte.

The electrolyte will be saturated with gaseous CO_2 (see section 2.2.3), such that the production of new gaseous products immediately leads to over-saturation of the electrolyte. We assumed that the formation of gaseous products Q_{gas}, is equal to the volume flux according to the ideal gas law

$$Q_{\mathrm{gas}} = \frac{i A_{\perp} R T}{n F p}. \tag{12}$$

Where R is the ideal gas constant, T the absolute temperature, n the stoichiometric number of electrons involved in the reaction, F the Faradaic constant, and p the pressure. We require that the volume flux of the electrolyte is much higher than the volume flux of produced gas, such that

$$Q_{\mathrm{electrolyte}} \gg \frac{i A_{\perp} R T}{n F p}. \tag{13}$$

The concentration of gaseous products will therefore not reach far beyond the saturation concentration, so that the gas bubbles will grow slowly [27, 63, 7]. Thus we assumed that small bubbles would be effectively advected out of the electrode, due to the drag force on the bubbles generated by the flow. [40]. Therefore, we approximated the velocity of the gas bubbles to be equal to the velocity of the electrolyte. The gas fraction can then be approximated in terms of volume fluxes, such that [9]

$$\epsilon_{\mathrm{gas}} = \frac{V_{\mathrm{gas}}}{V_{\mathrm{electrolyte}} + V_{\mathrm{gas}}} \approx \frac{Q_{\mathrm{gas}}}{Q_{\mathrm{electrolyte}} + Q_{\mathrm{gas}}}. \tag{14}$$

Where $V_{\mathrm{electrolyte}}$ is the volume of the electrolyte in the electrode and V_{gas} is the volume of the gas in the electrode.

2.2 Electrochemical reduction of CO_2 to CO

In this section, we discuss the chemical and electrochemical aspects of the CO_2R to CO of our setup. Those are the catalyst, half-reactions, the electrolyte, mass transport and potentials. The combinations of these factors will determine if, and how effectively the CO_2 can be reduced to CO. These aspects are influenced by each other and by the design of the FTE. In this project, we did not aim to find the best combination of catalyst and electrolyte. Instead, we investigated the well studied Ag catalyst and CO_2-saturated potassium carbonate catholyte, $KHCO_3$, for CO_2R to CO in a FTE.

2.2.1 Catalyst

Ag is a good catalyst because of its high selectivity towards CO. We tabulated the Faradaic efficiency (FE) values of Au, Ag and Zn in table 1, because they form CO as major product. The binding energy between these metals and $\cdot$COOH is sufficient for further reduction into $\cdot$CO intermediate. The intermediate is bound too weak to the metal and de-absorbs as CO from the electrode [24]. The price difference between Ag (520 euro kg^{-1}) and Au (45,000 euro kg^{-1}) [2], made Ag in our view a better choice. The porous electrode is made of a Ti substrate, as Ti is more abundant and cheaper than Ag [3]. Since it is difficult to fully cover the Ti electrode surface with Ag by electrodeposition (see section 2.3), Ti is also added to the table. The values in the table

only give an indication for the selectivity of these metals under the conditions mentioned. As the selectivity depends for example also on the morphology of the catalyst, the electrolyte, and the applied potential.

Table 1: Activity of Ag, Ti, Au and Zn in 0.1 M $KHCO_3$, at 18.5 ±0.5°C. Ti has a neglible selectivity towards CO.
Data taken from Hori et al. [25]

Catalyst	Potential vs SHE V	Current density mA cm^{-2}	FE			
			CO	H_2	$HCOO^-$	Total
Ag	-1.37	5.0	81.5	12.4	0.8	94.6
Ti	-1.60	5.0	tr.	99.7	0.0	99.7
Au	-1.14	5.0	87.1	12.4	0.7	98.0
Zn	-1.44	5.0	79.1	9.9	6.1	95.4

pH

Recent studies demonstrated that CO_2R favours a bulk pH in the vicinity of 7. Deviating too much will increase the Nernstian losses [51]. Significantly lower pH are favourable for HEV [24]. A higher pH in the bulk is generated by a higher concentration of $KHCO_3$ (see section 2.2.3). The local pH at the cathode is higher than that in the bulk, due to the production of OH^-, which could participate in restraining HEV reaction (see eqs. (15) and (16)) [36].

Oxygen evolution

Although we focused on the cathode side, the anode side needed to be taken into account as well. We used a Ni-based catalyst. Ni is a well known and cheap oxygen evolution catalyst. Unfortunately, Ni shows negligible activity in neutral pH conditions, since it favours a higher pH [62]. Much progress has been made to develop an oxygen evolution catalyst for neutral pH, but to date, there is none with a high performance [54, 56, 69, 77].

Bipolar membrane

To facilitate the possibility of working at different pH conditions, we used a BPM (Fumaseps FBM from Fumatech GmbH). An additional benefit from the BPM is that is works as an effective barrier against crossover of other ions from the anolyte to the catholyte and vice versa. This way, it prevents contamination of the catalyst from the other side [67]. For example, dissolved Ni ions can not contaminate the Ag catalyst. Adversely, the BPM forms an extra resistance. Shen et al. [49] measured that Fumaseps BPM has a voltage drop across the membrane of about 1.2 V at a 100 mA cm^{-2}. They also mentioned that above 600 mA cm^{-2} the BPM endures irreversible damage. On top of that, the BPM will also increase the price of the cell. To compensate for the voltage drop over the BPM, there is a decrease in cell potential when a pH gradient is provided over the BPM [67].

2.2.2 Half-reactions

In this section we cover the half-reactions on the cathode and on the anode side in an aqueous electrolyte for CO_2R to CO. HEV is the competing half-reaction at the cathode side of the CO_2R to CO. Wang et al. [68] concluded in their studies that CO_2 (aq) is the only electroactive carbon species responsible for CO_2R to CO, it is not the HCO_3^- nor CO_3^{2-}, which are present in the electrolyte as well (see section 2.2.3). The reaction includes either H^+ or OH^- ions depending on whether the reaction takes place in acidic or basic conditions. We operate the cathode side in neutral conditions, further discussed in section 2.2.3. The CO_2R reaction to CO will therefore read [24]

$$\mathrm{CO_2(aq) + H_2O(l) + 2\,e^- \rightleftharpoons CO(g) + 2\,OH^-} \quad \text{(-0.52 V vs SHE pH 7).} \tag{15}$$

The competitive HEV reaction is given as [24]

$$\begin{aligned} 2\,H_2O\,(l) + 2\,e^- &\rightleftharpoons H_2(g) + 2\,OH^- \\ &\text{(-0.414 V vs SHE pH 7).} \end{aligned} \tag{16}$$

Oxygen evolution at basic conditions is given by [57]

$$\begin{aligned} 4\,OH^- &\rightleftharpoons O_2(g) + 2\,H_2O(l)^+ + 4\,e^- \\ &\text{(0.4 V vs SHE pH 14, 0.8 V vs SHE pH 7).} \end{aligned} \tag{17}$$

The total half-reaction for CO_2R to CO will read

$$\begin{aligned} CO_2\,(g) &\rightleftharpoons CO\,(g) + 0.5\,O_2(g) \\ &\text{(-1.2 V pH 7).} \end{aligned} \tag{18}$$

Added to the half-reactions of eqs. (15) to (18) is the formal potential at a certain pH, as the formal potential is dependent on pH.

2.2.3 Electrolyte

The electrolyte composition influences both conductivity and selectivity. These, in turn, affect the electrochemical performance of the electrolyser. We will first explain the composition of the electrolyte. The influence of the concentrations of CO_2 is explained in section 2.2.5. Further, we will discuss the conductivity and the effect of cations.

Composition

We use a CO_2-saturated aqueous $KHCO_3$ solution. This is a well studied electrolyte for CO_2R to CO. We accomplished this by purging CO_2 through a KOH solution. KOH totally decomposes [22],

$$KOH \longrightarrow K^+ + OH^-, \tag{19}$$

so it forms an alkaline salt solution. We assumed that the bulk will reach an equilibrium, where the physically absorbed CO_2 is saturated. As $CO_2(g)$ dissolves in water, it exists in different inorganic forms; as physically adsorbed carbon dioxide, $CO_2(aq)$, as true carbonic acid, H_2CO_3, as bicarbonate, HCO_3^-, and as carbonate ions, CO_3^{2-} [30]. The $CO_2(aq)$, represents the physical absorption and the others are chemical absorption. The equilibria that form are described by Zeebe et al. [73].

$$CO_2(aq) + H_2O \rightleftharpoons H_2CO_3 \rightleftharpoons HCO_3^- + H^+ \rightleftharpoons CO_3^{2-} + 2\,H^+. \tag{20}$$

An equilibrium is reached when using both a KOH or a $KHCO_3$ solution. Since the concentration of H_2CO_3 is much lower than that of $CO_2(aq)$, these two are in literature usually denoted together as CO_2. We will adopt this notation in this report, such that

$$CO_2 = CO_2(aq) + H_2CO_3. \tag{21}$$

This will reduce the equilibria of eq. (20) to

$$CO_2 + H_2O \overset{K_1}{\rightleftharpoons} HCO_3^- + H^+, \tag{22}$$

which has slow reaction kinetics [24], and

$$HCO_3^- + H^+ \overset{K_2}{\rightleftharpoons} CO_3^{2-} + 2\,H^+. \tag{23}$$

Note that these are the equilibrium reactions, not the reaction pathways. So hydroxylation of CO_2 is not given in the equilibrium, even though it will happen in a basic solution. K_1 and K_2 are the equilibrium constants. Since $KHCO_3$ is a salt solution we use stoichiometric equilibrium constants, K_1^* and K_2^*, which depend on pressure p, temperature T, and salinity S. The remaining equations and constants used to determine the equilibrium concentrations are given in appendix A.1.

Conductivity

The concentrations in the electrolyte determine the conductivity κ [8],

$$\kappa = F \sum |z_\mathrm{i}| u_\mathrm{i} C_\mathrm{i}, \tag{24}$$

where u_i is the electrical mobility of the ion (given in table 5)of the individual ions, z_i is the charge of component i and C_i is the concentration of component i.

Cation effect

There is a diverse view on how cations influence the CO selectivity [42, 32]. Chen et al. [12] mentioned that K^+ cations would lower the overpotential for CO production. However, Lee et al. [34] reported a higher selectivity of the Ag catalyst towards CO at lower concentrations of K^+. Concentrations higher than 0.1 M $KHCO_3$ favor HEV over CO_2R, due to the masking of the electric field in higher electrolyte concentrations, which would destabilise the CO_2R intermediates [50]. The negative effect of K^+ cations on the CO_2R is due to their relatively small size, because decreasing cation radii would increase the HEV [58, 51]. So increased $KHCO_3$ concentrations could have a negative influence on the activity towards CO.

2.2.4 Mass transport and its limitations

Overcoming the mass transport limitations was an important reason for us to use the flow-through design for CO_2R to CO. Mass transport limitation is caused by a limited supply of reaction components to the electrode-electrolyte interface. In the case of CO_2R, the reaction component is CO_2.

Mass transport is determined by the Nernst-Planck equation [8],

$$\boldsymbol{J}_j = -D_j \boldsymbol{\nabla} C_j - \frac{z_j}{RT} D_j C_j \boldsymbol{\nabla} \phi + C_j \mathbf{v} \tag{25}$$

Here $\boldsymbol{J}_j$ is the flux of component j, in our case CO_2. The first term on the right side represents diffusion, the second term is migration, and the third is convection. Since CO_2(aq) has no charge, we assumed the migration to have no influence on the transport of CO_2(aq). The values of the diffusion coefficient, D_j, for CO_2(aq), OH^-, HCO_3^-, and CO_3^{-2} are listed in table 5.

Close to the electrode surface, the mass transport is predominantly driven by the diffusion perpendicular to the concentration gradient. Diffusion was used to determine the diffusion limited current density per internal surface area [66],

$$i_\mathrm{in,dif} = nFD \frac{C_\mathrm{bulk}}{\delta_D}, \tag{26}$$

when the current is only limited by diffusion. Here, we assumed a linear concentration gradient over the concentration boundary layer thickness, δ_D. In a limiting condition, the concentration on the cathode interface would be zero and the concentration at the end of the boundary layer would be equal to the concentration of the bulk C_bulk.

To determine the boundary layer thickness in the porous electrode, we simplified the flow through the porous electrode as a Poiseuille flow through a channel with a height of d_pore. Vedharathinam et al. [66] used a Leveque approximation to determine the δ_D. Our d_pore was already much smaller than this approximated value. We therefore approximated the δ_D to be equal to d_pore, which will probably be smaller. This way we were sure to not overestimate $i_\mathrm{in,dif}$. When advection and diffusion are in the same direction or at the same length scale, the Péclet number could be used to determine whether advection or diffusion would limit the current density. Since there is axial advection and radial diffusion, a variation introduced by Kenkel and Bard [28],

$$\frac{\text{advection transport rate}}{\text{diffusion transport rate}} = \frac{d_\mathrm{pore}^2 v_\mathrm{pore}}{DL}, \tag{27}$$

is more appropriate, which is equal to the Graetz number for mass transfer. When this ratio is much smaller than 1, it was referred to as high conversion efficiency, which means advection would be limiting. At increasing current densities, there would be depletion of the CO_2(aq). To make sure depletion would not occur, the advection transport rate should be bigger than the rate of consumed CO_2(aq), such that

$$C_{CO_2} v_s \gg \frac{i_{CO_2}}{Fn}, \tag{28}$$

where i_{CO_2} is the partial current used to reduce CO_2. The flow will not be diffusion mass transfer limited when

$$i_{in}(x) \ll i_{in,l}. \tag{29}$$

2.2.5 Potential and overpotential

The potential determines the energy needed to drive the reaction. The potential difference is measured from one point to another. In this section we determine the half potential as [8]

$$E = E_{0'} + \frac{RT}{nF} \ln \frac{C_O}{C_R} + \eta. \tag{30}$$

We measured the potential difference from the connection, where the electrons are supplied, to the surface of the electrode, closest to the anode. The first term of eq. (30) is the formal potential, $E_{0'}$. Together with the second term, they form the Nernst equation. The concentrations of the oxidised component C_O, and reduced component C_R, are taken equal to the bulk concentrations. The overpotential losses needed to drive the reaction at a certain current density are represented by η. In our FTE, these losses are caused by the ohmic overpotential, η_{ohm} and the activation overpotential η_{act}. At first, we determine the ohmic overpotential, taken equal to ionic overpotential [8], such that

$$\eta_{ohm} = \eta_{ion}(x) = \frac{\int_0^x i_m(x)dx}{\kappa_{eff}}, \tag{31}$$

where the electronic overpotential is neglected. This is a valid assumption, since the electronic conductivity σ (=2.1 $\times 10^6$ S m^{-1}[1]), is multiple orders higher than the ionic conductivity κ, which is a characteristic of the electrolyte (see section 3.1). To correct for the effect of the porous material on the conductivity, we use the effective ionic conductivity κ_{eff} [9],

$$\kappa_{eff} = \kappa \epsilon^{n_\kappa} (1 - \epsilon_{gas}(x))^{n_\kappa} \tag{32}$$

where ϵ^{n_κ} is the Bruggeman correction factor, and n_κ is approximated by 1.5 [21]. When the bubbles are effectively advected out of the electrode and eq. (13) holds, ϵ_{gas} can be neglected.

The activation overpotential is dominant at the electrode-electrolyte interface [8],

$$\eta_{act}(x) = b \ln \frac{i_{in}(x)}{i_0} \tag{33}$$

is derived from the Tafel equation, a simplification of the Butler-Volmer equation, which can be found in Bard and Faulkner [8]. Here i_0 (=$10^{-7.3}$ A m^2) is the exchange current density and b (=0.117 V) is an empirical Tafel constant for CO_2R to CO. We obtained their values from the Tafel slope determined by Lui et al. [35] in a 0.1 M $KHCO_3^-$ solution. The exchange current density,

$$i_{0,i} = C_i n_i k_i F [41], \tag{34}$$

is a function of C_i, n_i, and k_i, which is the concentration of the reactant, the charge transfer coefficient, and the reaction constant of species i respectively, in our case CO_2(aq).

2.3 Electrodepositing Ag on microporous Ti

The goal was to deposited Ag homogeneously on the Ti electrode, in order to provide sufficient catalytic area over the whole internal surface of the electrode, without blocking the pores.

2.3.1 Reactions

Electrodeposition happens when Ag ions are reduced at the cathode [26],

$$\mathrm{Ag^+ + e^- \rightleftharpoons Ag\,(s)}. \tag{35}$$

At the anode, formation of silver oxide $\mathrm{Ag_2O\,(s)}$, takes place [53],

$$\mathrm{2\,Ag^+ + 2\,OH^- \rightleftharpoons Ag_2O\,(s) + H_2O\,(l) + 2\,e^-}, \tag{36}$$

as well as the oxygen evolution reaction(see eq. (17)).

2.3.2 Particle growth

When a Ag ion reduces to solid Ag, it either forms a new small particle, called a nucleus, or it is deposited on an already formed Ag particle, so that the particle grows. Vanrenterghem et al. [64] characterised the difference in particle growth between high and low voltage, and so the difference between high and low current. They used a double pulsed method. During the first pulse, a high potential, $\sim$ 0.8 V vs. Ag/AgCl reference electrode, was applied, which causes nucleation of the Ag particles on the Ti cathode. A second pulse of low potential, $\sim$ 0.35 V vs. Ag/AgCl reference electrode, enabled particle growth. Be aware that these potentials were specifically determined for the setup used in that paper. Nevertheless, it was concluded that high potentials facilitate nucleation and low potentials particle growth. Also, they observed that a long second pulse leads to the agglomeration of the particles.

In order to prevent blockage of the pores, the deposited particles should be much smaller the micropores. This way, nucleation is favoured over particle growth or agglomeration, in order to reduce the size. Therefore, operating at higher potential, and consequently current, is favoured.

2.3.3 Deposition in porous electrode

The distribution of the current is proportional to the distribution of the Ag that is deposited. In order to have deposition on the whole internal area of the electrode, we require sufficient internal current densities over the whole thickness electrode. The distribution of the internal current during electrodeposition in a porous electrode is more uniform in x direction at low current densities (see section 3.2). For this reason, operating at low current densities is favourable. Also, a high conductivity would help to distribute the current more equal over the electrode thickness. To make sure that depletion $\mathrm{Ag^+}$ ions is avoided, Ag could be filled in eq. (28) instead of $\mathrm{CO_2}$.

Nevertheless, the current density required for uniformity in x direction conflicts with the current density required for depositing small particles. This required optimisation of the current density, thus the potential, during electrodeposition of Ag on microporous Ti.

2.3.4 High pulse electrodeposition

We hoped to overcome the unequal distribution of current by high pulse electrodeposition. High pulse electrodeposition has proved to be an effective trigger for the nucleation of particles in the bottom of the pores [37, 11, 44]. The deposition pulses are short enough to avoid diffusion limitations, since the diffusion layer does not have sufficient time to develop. Therefore, high pulse can overcome mass transport limitations. Nevertheless, high pulse electrodeposition can not overcome the unequal distribution of current by the electrode ohmic overpotential. This is due to the fact that electro-neutrality happens in a matter of nanoseconds and thus the distribution of current by the ohmic overpotential as well [15].

2.3.5 Deposited volume

The deposited volume of Ag can be defined as [9]

$$V_{\mathrm{ag}} = \frac{Q M_{\mathrm{Ag}}}{n_{\mathrm{Ag}} F \rho_{\mathrm{Ag}}}, \tag{37}$$

where Q is the charge used for the deposition, M_{Ag} is the molar mass of Ag ($= 107.87$ g mol^{-1}), n_{Ag} is the stoichiometric constant during Ag reduction, and ρ_{Ag} is the density of Ag ($= 10.49$ g cm^{-3}).

We can express the charge per unit area as a function of the current density using conservation of charge, such that

$$\frac{Q}{A} = \int_0^{t_{\text{depo}}} i(t)\, dt, \tag{38}$$

where t_{depo} is the deposition time. As we did not expect the Ag particles to deposit as a flat homogeneous layer, we combined eqs. (11), (37) and (38) to determine the volume fraction of Ag as a function of x, such that

$$\epsilon_{\text{Ag}}(x,t) = \frac{aM_{\text{Ag}}}{n_{\text{Ag}}F\rho_{\text{Ag}}} \int_0^{t_{\text{depo}}} i_{\text{in}}(x,t)\, dt. \tag{39}$$

This fraction should be much smaller than the void fraction, such that the electrolyte flow is not obstructed by the deposited Ag.

3 Modelling

Through modelling, we hoped to get a better understanding of the conditions in the cell, especially those at the electrolyte-electrode interface. We expect these conditions to change over the thickness of the electrode. We hope to accomplish a better understanding of the mechanisms that determine the performance of the FTE. To determine the performance of the FTE, we can alter the concentration of the electrolyte $C_{\mathrm{KHCO_3}}$, particle diameter d_p, electrode thickness L, void fraction ϵ_{void}, and the superficial velocity of the electrolyte v_s, to some extend. In this section, we first plotted the bulk concentrations, which are a function of the concentration of the electrolyte $C_{\mathrm{KHCO_3}}$. After that, we modelled the diffusion mass transport limiting current density $i_{\mathrm{in,dif}}$, the current distribution $i_{\mathrm{in}}(x)$ and $i_{\mathrm{m}}(x)$, the convection current i_{con}. We plotted most of the outcomes in graphs to highlight the relation between important parameters. Most of the equations used in this section are already given in section 2.3.5. In all the graphs, atmospheric pressure ($p = 101{,}325$ Pa) and room temperature ($T = 298$ K) was assumed.

3.1 Electrolyte bulk conditions

We used the equilibrium conditions, given in appendix A.1, to describe the bulk conditions in the cell. The CO_2 concentration was determined using eq. (45). Together, eqs. (41), (44), (51) and (52) form four equations with four unknowns. Namely, $C_{\mathrm{OH^-}}$, $C_{\mathrm{HCO_3{}^-}}$, $C_{\mathrm{CO_3{}^{2-}}}$ and $C_{\mathrm{H^+}}$. We solved this set of equations for a $KHCO_3$ solution in the range of 0 to 1 M. The bulk condition are visualised in fig. 2.

As can be seen in fig. 2b, is the CO_2 not changing so much in this concentration range and would not be leading to determine the $KHCO_3$ concentration. More importantly would be the electrolyte conductivity, which changes more significantly within this range, as shown in fig. 2c. Also, the pH is changing a lot (see fig. 2b), especial at the lower concentration. In those low pHs, HEV would be favoured.

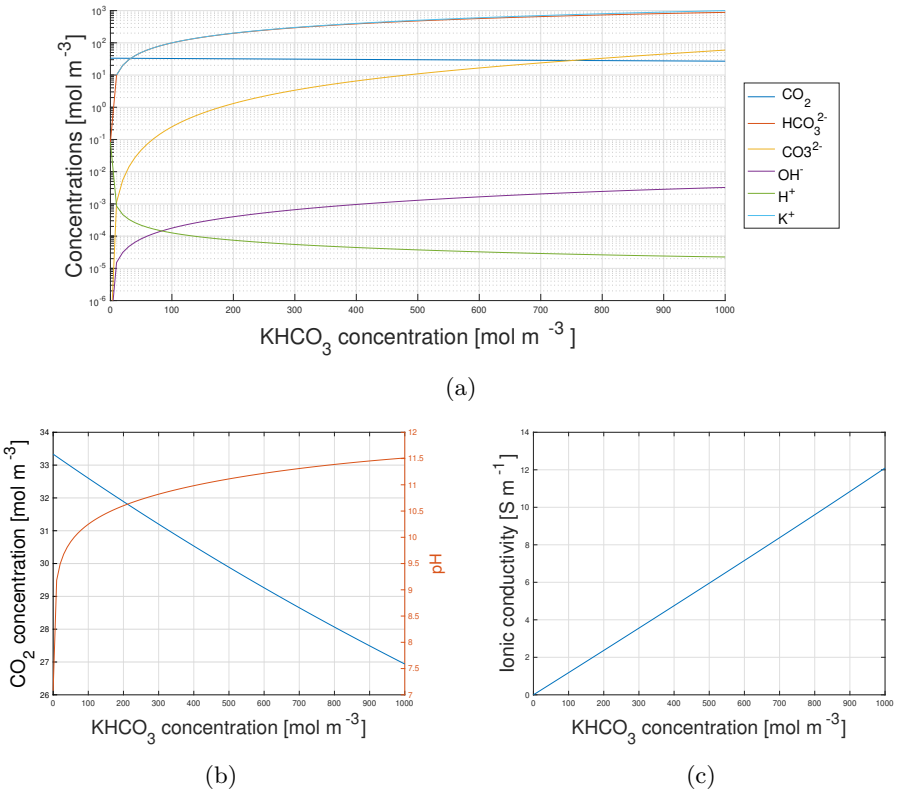

Figure 2: The bulk conditions of a CO_2-saturated $KHCO_3$ solution plotted over a range 0-10 M. (a) plots the concentration of the dissolved components. (b) shows that the concentration of physically absorbed CO_2 is not changing that much in this range, but the pH is very at low concentrations. (c) plots the ionic conductivity, which is rising linearly from the origin

3.2 Current distribution

To model $i_{\mathrm{m}}(x)$ and $i_{\mathrm{in}}(x)$, we used a similar derivation as Newman and Tobias [43]. The derivation to obtain the mathematical description of the current density can be found in appendix A.2. We plotted the distributions of $i_{\mathrm{m}}(x)$ and $i_{\mathrm{in}}(x)$ of a 2 mm thick electrode, in a 0.1 M $KHCO_3$ in fig. 3. The distribution is much dependent on the i of the cell, which can be seen infig. 3. The higher i of the cell the more the reactions happen closer to the counter electrode. The same happen when the $KHCO_3$ concentration decreases (see fig. 9). The $i_{\mathrm{in}}(x)$ is linear dependent on d_{p} (see eq. (60)), so the values of fig. 3b can be easily be adapted for the d_{p}. The $i_{\mathrm{m}}(x)$ is independent from d_{p}. A decrease in d_p will therefore only lower the activation overpotential, not the ohmic.

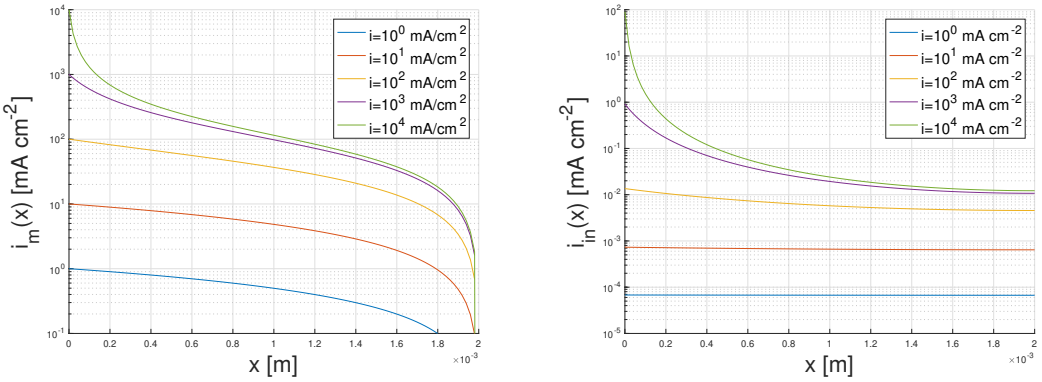

(a) (b)

Figure 3: Plots (a) $i_{\mathrm{m}}(x)$ and (b) $i_{\mathrm{in}}(x)$, of a 2 mm thick electrode, in a 0.1 M C_{02}-saturated $KHCO_3$ solution at different cell current densities i. The distribution of $i_{\mathrm{m}}(x)$ and $i_{\mathrm{in}}(x)$ are more homogeneous at lower cell current densities.

3.3 Limiting current by diffusion and convection

The diffusion limited current density per internal surface area, $i_{\mathrm{in,dif}}$, is approximated by eq. (26) and plotted in fig. 4a. The values in this plot can be compared with the $i_{\mathrm{in}}(x)$. The highest value for $i_{\mathrm{in}}(x)$ is found at $x = 0$, so therefore we can check fig. 3b at $x = 0$ to see if $i_{\mathrm{in}}(x)$ is far away from mass transport limitations.

We expressed the limiting convection current density $i_{\mathrm{l,con}}$, as the cell current density that would be used, when al the convected CO_2 would get reduced. The $i_{\mathrm{l,con}}$ is plotted in fig. 4b. These values need to be compared with the cell current i. We see that when the electrolyte has a superficial velocity of 0.5 mm s^{-1}, the convection current is not that high, which could to a significant decrease in the bulk concentration at the end of the electrode.

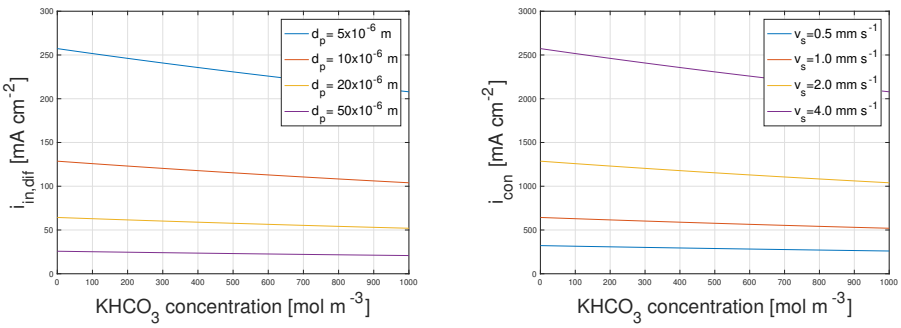

(a) (b)

Figure 4: (a) negative linear relation between the electrolyte concentration and the diffusion limited internal current densities with a diffusion layer thickness of 5 μ m. (b) cell current density when it would be limited by convection at different superficial velocities.

3.4 Local condition

The local condition at the electrode interface depends on the diffusion current (see eq. (63)), the boundary layer thickness, and the bulk conditions. Local migration and diffusion can be approximated by the relations given in appendix A.3. Although both i_{in} and Δ_D are smaller than conventional electrolysers, this can still cause a significant difference between the bulk and local concentrations. This can be seen in the local OH^- concentration and local pH, shown in fig. 5. The is mostly significant because the OH^- concentration in the bulk is relative low, compared to the concentration difference due to diffusion. The local high pH is good for suppressing the HEV reaction, but high concentration can also have negative effects on the activity towards CO table 1.

Due to migration and diffusion, the local K^+ concentration will be lower than the bulk K^+ concentration. But due to the relative high concentration in the bulk, the local K^+ concentration does not deviate significantly, see fig. 10.

For this calculations, we assumed that the concentration boundary layer thickness was equal to the pore size. We expect the thickness, in reality, to be smaller than the pore size and therefore the concentration to deviate less from the bulk conditions. We expect the local pH therefore also to be smaller than the one we have calculated.

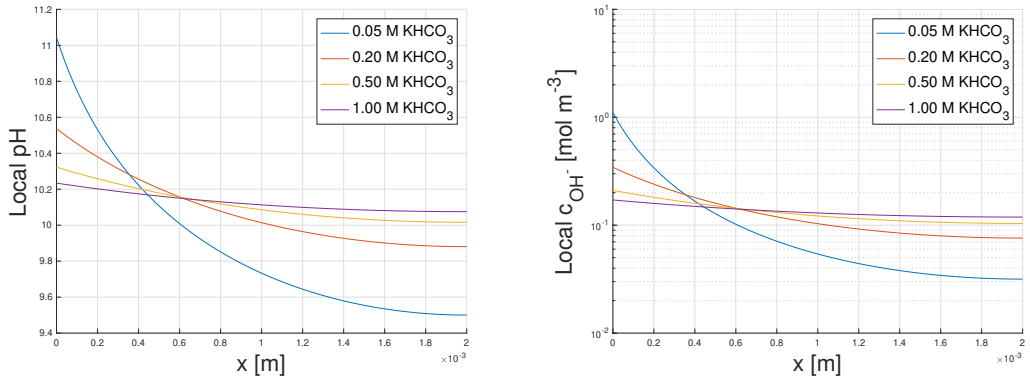

(a) (b)

Figure 5: (a) show the Local pH over the x coordinate at different electrolyte concentrations. (b) shows the deviation of local OH^- concentration from the bulk. Both the graphs are shown for at a cell current density of 200 mA m^{-2} Interestingly is that the local pH is higher at smaller x, due to higher local production of OH^- ions at higher internal current densities.

4 Materials and Methods

We used the almost same FTE for the CO_2R to CO experiments (see fig. 6), as for the electrodeposition experiments (see fig. 14a). First, we performed electrodeposition to obtain a sufficient Ag coverage of the Ti electrode surface. Subsequently, we evaluated the quality of the deposited layer and the performance of the whole FTE. We performed the experiments always in this sequence. To support the experiments, we performed a scanning electron microscopy (SEM) analysis, flow velocity tests, pH measurements, gas chromatography (GC) analysis, high-performance liquid chromatography (HPLC), and inductively coupled plasma optical emission spectroscopy (ICP-OES) analysis. We first discuss the porous Ti electrode, then the rest of the setup that we used. After that, we explain the electrodeposition and the CO_2R to CO. In appendix A.4 you will find the instruments we used.

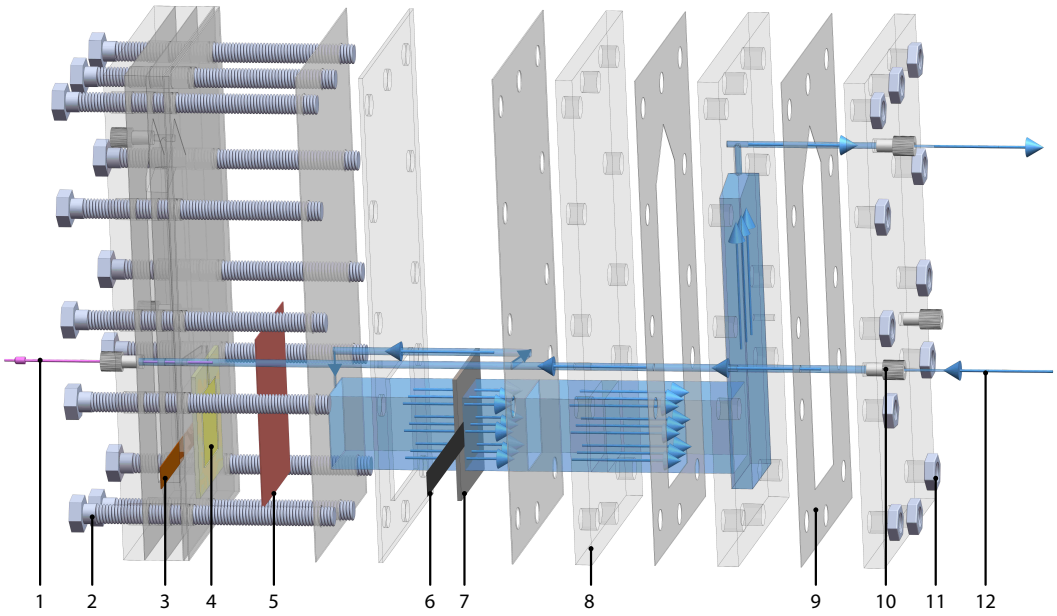

Figure 6: A SolidWorks render of the experimental setup of the $CO2R$ to CO, in realistic proportions. Exploited view of the cathode side. Some colours differ from reality to distinguish the different components. The flow of the electrolyte is visualised in blue.

4.1 Porous Ti electrode

We used Ti electrodes that were sintered by Baoji Along Filtration Material Science & Technology Co., Ltd. The dimensions of the electrodes are shown in table 2. Here L is the thickness of the electrode, w represents the height and width of the flow-through channel, and d_p is the nominal particle diameter. The outer dimensions of the electrode were $50 \times 50 \times 1$ mm. A band of 10 mm around the whole perimeter was used to clamp the electrodes between gaskets. The remaining area, 30×30 mm, was available for the electrolyte to flow through. Two electrodes with a thickness of 1 mm were placed on top of each other in order to form a single electrode with a thickness of 2 mm. This way, we could inspect the surface in the middle of the electrode, after electrodeposition or CO_2R to CO, with the SEM.

Table 2: Dimensions of the electrode , with L as the electrode thickness, w the width and height of the electrode and d_{p} the size of the sintered particles.

Electrode number	L ($\times 10^{-3}$ m)	w ($\times 10^{-3}$ m)	d_p ($\times 10^{-6}$m)
1	2	30	5
2	1	30	5
3	2	30	10
4	2	30	20

4.2 Setup

We will first describe the FTE that we utilised for the CO_2R to CO, and then we will explain the little difference to perform the electrodeposition. The setup is visualised in fig. 6, in realistic proportions. To give an impression of the size, the plates are 200 × 110 mm. To show the place of the components, we made an exploded view of the cathode side. The colours of the parts may differ from reality to distinguish from the other parts. The different number are assigned to the parts in the figure and correspondent with the numbers in the text. We added the flow path of the catholyte (# 11), which enters at the right side, flowing via a 3 mm channel to the left side of the cathode. It flows through the Ti cathode and exits at the right side at the top. The flow path of the anolyte is the same but mirrored over both vertical planes halfway the cell. PMMA plates (#8) formed the structure of the cell. Laser-cuts in the PMMA created the path of the electrolyte and connected other parts. The 0.2 mm thick silicone gaskets (#9), in between the plates, made the cell leak-tight. In one of the plates, the cathode (#7) was fitted. To connect the cathode to the outside, we used a 0.1 mm thick Ti sheet (#6), so electrons can be supplied to the cathode. The BPM (#5, see section 2.2.1) was clamped between two gaskets. The Ti cathode and on the other side the Ni anode (#3) are directly pushed against the silicon gaskets. Cuts in the gaskets leave space for the electrolytes to flow between the electrodes and the BMP. This way, we attempted to minimise the distance between the electrodes. A 0.1 mm copper sheet (#5) connects the Ni anode with the outside, so electrons exit the anode. The Ag/AgCl reference electrode (#1) is placed at the dead-end of the channel, opposing to the entrance of the catholyte. So it can measure potential in the catholyte stream at the BPM side of the cathode. The screw connections (#12) form a leak-tight bond with the tubes that transport the electrolyte, and to connect the reference electrode. Twelve bolts (#2) and nuts (#11) clamped the plates together.

However, the electrodeposition cell (see fig. 14a) has on the position of the BPM a PMMA plate that supplies one electrolyte to both the cathode a the anode. The Ni anode was replaced by a Ti electrode with Ti sheet connection to the outside of the cell.

For the CO_2R to CO, we additionally used a bubble column (see fig. 14b), a gas-liquid separator (GLS) (see fig. 14c) and an anolyte reservoir. For the electrodeposition, we use a reservoir for the catholyte and one for the anolyte. A picture of the setup during one of the experiments can be seen fig. 14d.

4.3 Electrodeposition procedure

Before assembling the cell, the Ti electrode was submerged in 66 % nitric acid (HNO_3) for 20 minutes to dissolve and remove any contamination, or previous deposition layers from the electrode surface. Subsequently, the electrode was rinsed with demineralised water. The same washing procedure was used for the Ti connections. After cleaning the electrodes and assembling the cell, we also rinsed the cell with demineralised water.

We used a electrolyte that consist of 1.0 M lithium perchlorate $LiClO_4$(99.99 %, Sigma-Aldrich) as a supporting electrolyte, and 0.1 M silver nitrate $AgNO_3$ (>= 99.0 %, Sigma-Aldrich) to provide the Ag ions, in nano-pure water (0.055 ţS/cm). This electrolyte was successfully used to deposit Ag on Ti by Vanrenthergem et al. [**?**], they used lower concentrations. We increased $LiClO_4$ concentration to increase the conductivity and support a more equal distribution of $i_{\mathrm{in}}(x)$ over x. To eliminate the effect of mass transport limitation we increased the $AgNO_3$. We controlled the cathodic half cell potential using a BioLogic VSP-300 potentiostat [18]. After electrodeposition and rinsing with demineralised water, we used the SEM to inspect the front and rear side of the electrode. We studied the distribution and morphology of the deposited Ag particles using the

magnified images generated by the SEM. We analysed the quality of the particles by performing energy-dispersive X-ray spectroscopy (EDS) with the SEM. We examined the electrodeposition further during the CO_2R to CO.

4.4 CO_2R to CO

First, the catholyte flows through a bubble column, where it becomes saturated with CO_2. After that, the catholyte flows through the cathode side of the cell. At last, the gaseous products gets separated from the catholyte in the GLS, and the catholyte flows back to the bubble column. The gas is tested by performing GC analysis. The anolyte circulates from the reservoir to the flow-through cell and back to the reservoir. We used a three-electrode system for the CO_2R to CO as well. This was done by using the cathode after electrodeposition as working electrode again. The anode, counter electrode, was a sandwich of 5 layers of sintered Ni 10 μm wired felt. We used the Ag/AgCl reference electrode. As the anolyte, we used a 5.0 M KOH (90.0 %, VWR Chemicals) solution. This created a high conductivity on the anode side. For the catholyte, we used a 0.05 M, 0.2M and 0.5M CO_2-saturated $KHCO_3$ solution. Obtained by CO_2 purging KOH (90.0 %, VWR Chemicals) solutions , with the same concentrations. We used the BK Precision 9151 Programmable DC Power Supply to facilitate currents of up to 27 A. Unfortunately, we could only control the cell potential. The cathode side could not be controlled directly. We measured the cathodic potential and manually adapt the cell potential in order to achieve approximately the desired cathodic potential. We used two positive displacement pumps, which allowed us to create flow rates between 1.0 and 7.7 mm s^1

5 Results and Discussion

The combination of experiments, modelling, and theory provided useful insights into the characterization of the FTE for CO_2R to CO, using a Ag catalyst electrodeposited on a microporous Ti cathode. Though, it was hard to obtain consistent data during the CO_2R to CO. To produce CO partial current densities above 20 mA cm^{-2} was already challenging. Additionally, we will discuss CO_2 gas that was found in the output stream.

5.1 Electrodeposition

To form a homogeneous, thin, and covering layer of Ag on a porous Ti electrode was challenging. As explained in the theory, the deposition of small particles requires higher potentials than the homogeneous distribution of catalyst over the x-coordinate of the electrode. Shown in figs. 7a to 7c are SEM images of the front side of the electrode after electrodeposition was performed at high potential (4 V vs Ag/AgCl). In figs. 7d to 7f, the front side of the electrode after electrodeposition at low potential (0.8 V vs Ag/AgCl) is shown. This is representative of what we observed in general. At high potentials, we observed a homogeneous distribution of $\sim$ 1 μm Ag particles on the front side. At low potential, we observed that most of the area was covered by tiny Ag particles for less than 1%, see figs. 13a and 13b. However, in some locations, the Ag particles accumulated. A high density of Ag particles with a size of $\sim$ 5-15 μm was formed figs. 7d to 7f. A reason for this could be that local lower activation overpotentials are more significant when working at lower potentials.

Images of the front side of the cathode showed a much more homogeneous distribution of Ag particles at a higher voltage. Yet, the SEM images alone were not sufficient to determine the quality of the deposition, as they did not provide any information of the inside of the electrode. The backsides of all the electrodes looked equally empty, even at lower potentials than 0.8 V. Therefore, we questioned if the current distribution was the only reason for the non-uniform distribution of Ag particles over the x coordinate.

More important to determine the success of the deposition was the activity towards CO (see section 5.2). In general, we noticed a negligible activity towards CO at the low potential electrodeposited electrode. The activity towards CO was significantly better at the high potential electrodeposited electrodes, therefore we focused on deposition at higher potentials.

Nevertheless, we are aware that we did not test the full spectrum of possibilities to determine the characteristics of successful electrodeposition of a catalyst on a microporous electrode of this thickness. We expect that the electrodeposition on a microporous electrode can still be improved by further increasing the effective conductivity, by increasing the electrolyte concentrations and increasing the void fraction. Additionally, bigger pores would allow deposition of bigger Ag particles, but they have a negative influence on the CO_2R to CO (see section 5.2). Next to that, the used potential and deposition time can be optimized. Electrodeposition on thin substrates can improve the coverage of Ag particles over the x coordinate. A more effective, but also more complicated solution would be to perform the deposition of Ag particles on the Ti particles, prior to the sintering. This could ensure uniform deposition on each Ti particle, independent of their location in the electrode.

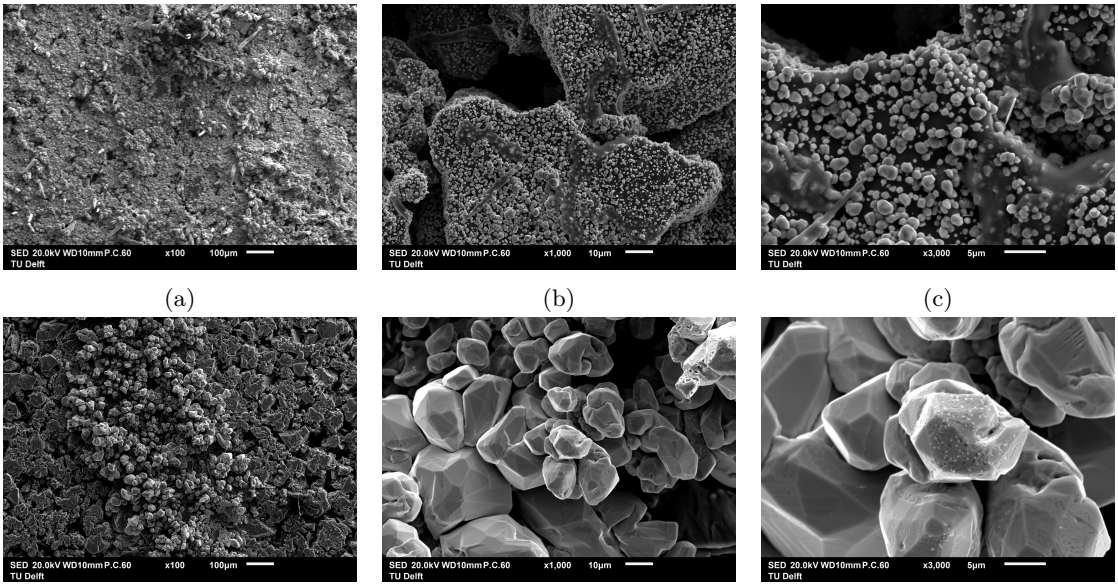

(a) (b) (c)

(d) (e) (f)

Figure 7: SEM images of the front side of the microporous Ti electrode after electrodeposition of the Ag particles, with an applied charge of 40 C. Figures (a), (b), (c) show the results when applying 4V cathodic potential at a magnification of 100, 1000, and 3000 times respectively. The Ag particles are about 1 μm. Figures (d, (e), (f) show the results when applying 0.8V cathodic potential at a magnification of 100, 1000, and 3000 times respectively. Here the Ag particles are about 5-10 μm.

5.2 CO_2R to CO

The results shown in fig. 8 are obtained from measurements with a high potential electrodeposited electrode, as the low potential electrodeposited electrodes showed no significant CO partial current density. The tests were performed using the same electrode, using a 0.05, 0.20 and 0.50 M CO_2-saturated $KHCO_3$ electrolyte with a superficial flow velocity of 4 mm s^{-1}. We measured the highest CO partial current density, 62 mA cm^{-2}, in 0.05 M $KHCO_3$. This was due to the higher selectivity towards CO at lower $KHCO_3$ concentrations, reaching an FE of 27 %.

This is in contrast with the lower pH at lower $KHCO_3$ concentrations, which should favour HEV. However, lower $KHCO_3$ concentrations are favourable, since K^+ cations negatively influence the activity towards CO (see section 2.2.3).

The lower FEs towards CO at lower current densities can be explained by the local pH [**?**]nd local K^+ concentration, which deviate more from the bulk at higher current densities fig. 5. The increase in local pH and the decrease in local K^+ concentration becomes stronger with increasing current density.

Nevertheless, the FEs that we obtained are not even half the FEs towards CO at a Ag catalyst that are shown in table 1. We believe that this was mainly caused by the insufficient deposition of Ag particles. We observed big differences in the activity towards CO between the different deposition attempts. The reproduction of electrodes that showed good results was difficult. During a one-off test, a CO partial current densities of 100 mA cm^{-2} was measured, at an FE of 55 % (see fig. 14).

The linear relation between the cell potential and the total current implies that most of the overpotential in the cell is due to ohmic losses (see fig. 8d). These can be ascribed to the low conductivity of the catholyte and the resistivity of the BPM.

Increasing the conductivity of the electrolyte concentration is not really an option when using a K^+ or smaller cation based electrolytes. Using electrolytes based on bigger ions could be an option to improve the ionic conductivity (see section 2.2.3). Ionic liquids seem to have promising characteristics as well [23, 55, 47].

Better performance in neutral pH of an oxygen evolution catalyst would make it possible for the FTE to work without the BPM. This would eliminate the ohmic potential drop over the BPM.

The measurements showed no sign of mass transport limitations, as altering the flow velocity

of the electrolyte through the electrode did not alter the FEs of CO. However, we observed lower total current densities at lower flow velocities. We expected that decreasing gas advection at lower flow rates would decrease the effective conductivity and therefore decrease the current densities. This questions the assumption of effective advection of gas that was made earlier, therefore requires more research.

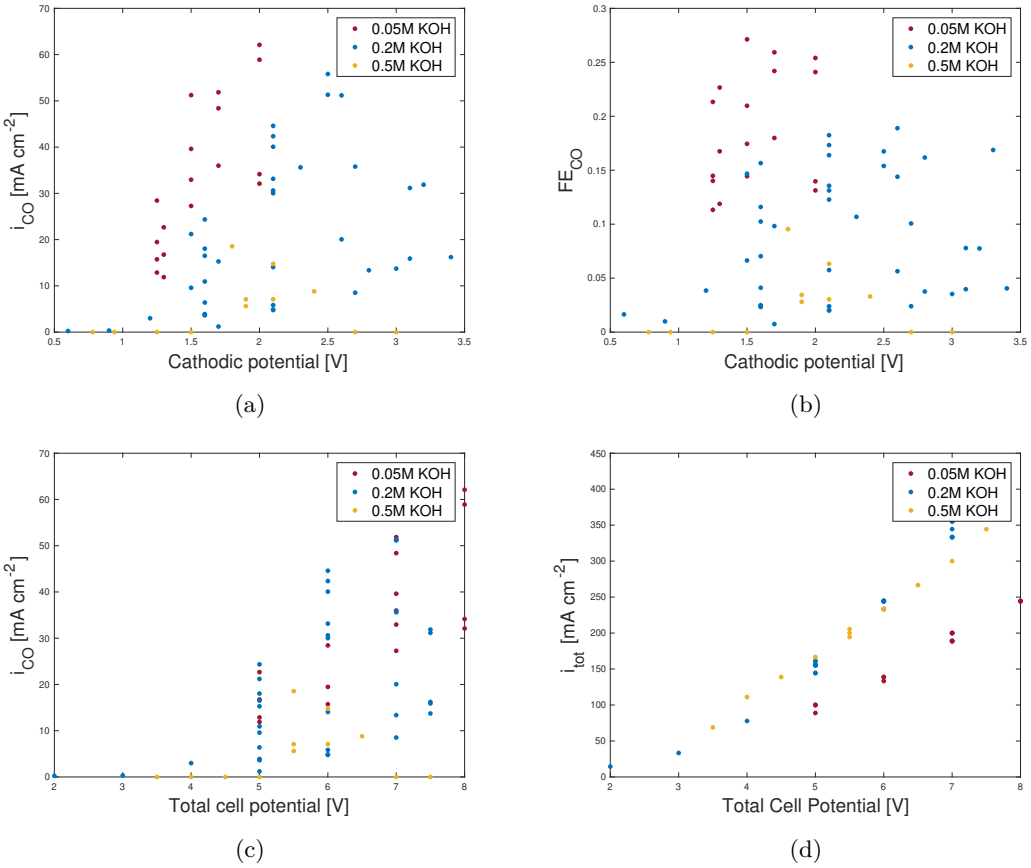

Figure 8: Experimental results of CO_2R to CO at different potentials in CO_2-saturated 0.05 M, 0.2 M and 0.5 M $KHCO_3$ solution. (a) Partial current density used for the production of CO vs. cathodic potentials. (b) FE towards CO vs. cathodic potentials. Both the CO partical current density and FE are the highest, when using a 0.05 M $KHCO_3 solution, 62 mA cm^{-2}$ and 27 % respectively. (c) Partial current density used for the production of CO vs. cell potentials. (d) Total current density vs. cell potential. Linear relations shows ohmic behaviour.

6 Conclusion

In this research, we proved that an FTE can produce CO partial current densities far beyond the mass transport limited current densities of conventional aqueous CO_2R to CO electrolysers. Conventional electrolysers are mass transfer limited to 20 mA cm^{-2}. Our FTE has reached a CO partial current density of up to 100 mA cm^{-2}. From observations and modelling, we reasoned that this flow-through design could exceed this current density much more in terms of mass transport, without requiring higher electrolyte flow velocities than the used 4 mm s^{-1}.

However, the setup suffered from low selectivities and high cell potentials, above 5 V, when producing significant CO partial current densities, of more than 20 mA cm^{-2}. The high potentials can be ascribed to ohmic losses and low selectivities towards CO.

A one-off FE of 55% was reached, and repeatable FEs of 25% were produced. We believe that the insufficient coverage of the Ag catalyst over the whole porous electrode was the main reason for these low FEs. The low potentials that were required to deposit the Ag particles homogeneously over the thickness of the porous Ti were conflicting with the high potentials needed to create particles smaller than the micropores. Further optimising the deposition potential and deposition time, while increasing the void fraction and conductivity, can improve the distribution of the Ag on a Ti microporous electrode. Alternatively, the Ag could be deposited on the Ti particles before sintering the particles together into a porous electrode. This could provide better control of the electrodeposition.

The ohmic losses were believed to be caused by the low conductivity of the electrolyte and the resistivity of the BPM. Increasing the conductivity by using a higher $KHCO_3$ concentration is not an option, due to the negative effect of the K^+ cations on the activity towards CO. The use of higher electrolyte concentrations would be possible when using a different electrolyte, for example, one that consists of bigger cations.

We believe that if that much improvement can be made the above-mentioned improvement could contribute to making a flow-through electrolyser a promising candidate to effectively reduce at an industrial scale.

Although our FTE suffered from low selectivity towards CO and high cell overpotentials, the FTE is still a promising candidate to effectively reduce CO_2 to CO at an industrial scale. We believe that the mentioned improvements, in both the electrodeposition and the CO_2R to CO, could improve the performance of the FTE significantly.

Appendices

A Appendix

A.1 Concentrations of components in the electrolyte

First we write the stoichiometric as

$$K_1^* = \frac{[\mathrm{HCO_3}^-][\mathrm{H}^+]}{[\mathrm{CO_2}]}, \tag{40}$$

and

$$K_2^* = \frac{[\mathrm{CO_3}^{2-}][\mathrm{H}^+]}{[\mathrm{HCO_3}^-]}, \tag{41}$$

which are determined by Millero et al. [39], such that

$$pK_i^* = pK_i^0 + A_i + \frac{B_i}{T} + C_i \ln T, \tag{42}$$

where A_i, B_i, and C_i are functions of the salinity S given in table 3. Water dissociation participates in these carbonate equilibria, with the corresponding stoichiometric equilibrium constant, given by

$$\mathrm{H_2O} \overset{\mathrm{K_W}}{\rightleftharpoons} \mathrm{H}^+ + \mathrm{OH}^-, \tag{43}$$

and

$$K_W^* = [\mathrm{H}^+][\mathrm{OH}^-]. \tag{44}$$

The saturation concentration of CO_2 is given by Henry's law,

$$[\mathrm{CO_2}] = p_{\mathrm{CO_2}} K_{\mathrm{CO_2}}, \tag{45}$$

here $p_{\mathrm{CO_2}}$ is the partial pressure of CO_2. Since we purged pure CO_2 through the electrolyte, only the saturation pressure of the water vapor, $p_{\mathrm{w,sat}}$, is considered in Dalton's law of partial pressure [59]

$$p = p_{\mathrm{CO_2}} + p_{\mathrm{w,sat}}, \tag{46}$$

Antoine's equation [59],

$$p_{\mathrm{w,sat}} = 10^{A - \frac{B}{C+T}} \times 133.322, \tag{47}$$

can be used to calculate $p_{\mathrm{CO_2}}$, using Antoine coefficients, A = 8.07131, B = 1730.63, and C = 233.426.

$K_{\mathrm{CO_2}}$ was adjusted by Weiss et al. [70],

$$\ln K_{\mathrm{CO_2}} = W_1 + W_2 \left(\frac{100}{T}\right) + W_3 \ln \frac{T}{100} + S\left(W_4 + W_5 \left(\frac{T}{100}\right) + W_6 \left(\frac{T}{100}\right)^2\right) \tag{48}$$

for the effect of salinity, S, and temperature, T. Where W_1, W_2, W_3, W_4, W_5 and W_6 are constants determined by Weiss et al. [70], their values are given in table 3.

Table 3: Tabulates constants that are used to determine the equilibrium of the electrolyte, where (a) pK_1^0, pK_2^0, $\ln K_w^*$,A_1, A_2, B_1, B_2, C_1 and, C_2 are given by Millero et al. [39] and (b) W_1, W_2, W_3, W_4, W_5, and W_6 are determined by Weiss et al. [70].

(a)

Variable	Expression
pK_1^0	$-126.34048 + \frac{6420.813}{T} + 19.56822 \ln T$
pK_2^0	$-90.18333 + \frac{5143.692}{T} + 14.613358 \ln T$
A_1	$13.4191 S^{0.5} + 0.0331 S - 5.33 E - 0.5 S^2$
A_2	$21.0894 S^{0.5} + 0.1248 S - 3.687 E - 0.4 S^2$
B_1	$530.123 S^{0.5} - 6.103 S$
B_2	$-72.483 S^{0.5} - 20.051 S$
$\ln K_w^*$	$148.96502 - 13847.26/T - 23.6521 \ln T$
	$(+118.67/T - 5.977 + 1.0495 \ln T) S^{0.5} - 0.01615 S$
C_1	$2.06950 S^{0.5}$
C_2	$3.3336 S^{0.5}$

(b)

Variable	Expression
W_1	-58.0931
W_2	90.5069
W_3	22.294
W_4	0.027766
W_5	-0.025888
W_6	0.0050578

The equilibrium constants are dependent on the initial salt concentration, in terms of the salinity. This can be calculated by [39]

$$S = \frac{1000 I}{19.924 + 1.005 I}, \tag{49}$$

using the ionic strength, I, given by [73],

$$I = \frac{1}{2} \sum C_i \cdot z_i^2, \tag{50}$$

where C_i is the concentration of the K^+ and the OH^- ions of the post CO_2-dissolution solution, z_i is the charge of these ions. These are general values independent of the type of salt used. The OH^- concentration is higher in the presence of K^+ than in the presence of Na^+ ions, as an example [45].

The equilibrium relations only hold for dilute systems, so we will vary the initial salt concentration from 0 to 1 M KOH, while applying the these equilibria. We will use 298.15 K and 1 atm as operating temperature and pressure respectively, which is within the valid range of the equilibria.

It is safe to say, that electroneutrality holds, since separation of charge will be in the order of nanoseconds and nanometres [15]. Electroneutrality becomes

$$z_{K^+}[K^+] + z_{OH^-}[OH^-] + z_{H^+}[H^+] + z_{HCO_3^-}[HCO_3^-] + z_{CO_3^{2-}}[CO_3^{2-}] = 0. \tag{51}$$

Reaction Rate

At last, we determine the reaction rates of the electrolyte, to indicate the time that is needed to reach an equilibrium. As the reaction kinetics of the equilibrium given by eq. (22) are much slower than those of the equilibrium given by eq. (23) [24], we consider eq. (23) to be in equilibrium continuously. All the rate constants are obtained by Schulz et al. [48] and tabulated in table 4. We also assumed the dissolved CO_2 to be always saturated according to eqs. (45) to (48). The rate at which CO_2 dissolves will read

$$\frac{\partial}{\partial t}[CO_2] = -[CO_2][OH^-] k_{1,f,H^+} + [HCO_3^-] k_{1,f,H^+}, \tag{52}$$

and can be used to determine the purge time and relevance of buffer effect in the electrode.

Table 4: Reaction rate constants determined by Schulz et al. [48].

Variable	Value	Unit	Expression
$k_{1,f}^{H^+}$	3.71×10^{-2}	s^{-1}	$\exp(1246.98 - 6.19 \times 10^4)/((T - 183.0)\ln(T))0$
$k_{1,b}^{H^+}$	2.67×10^4	kg mol^{-1} s^{-1}	$k_{1,f}^{H^+}/K_1^*$
$k_{2,f}^{H^+}$	5.0×10^{10}	kg mol^{-1} s^{-1}	None
$k_{2,b}^{H^+}$	59.44	s^{-1}	$k_{2,f}^{H^+} \times K_2^*$
$k_{1,f}^{OH^-}$	2.23×10^3	kg mol^{-1} s^{-1}	$A_4 \exp(-90166.83/(RT))/K_W^*$
$k_{1,b}^{OH^-}$	9.71×10^{-5}	s^{-1}	$k_{1,f}^{OH^-}(\ K_W^*/K_1^*)$
$k_{2,f}^{OH^-}$	6.0×10^9	kg mol^{-1} s^{-1}	None
$k_{2,b}^{OH^-}$	3.06×10^5	s^{-1}	$k_{2,f}^{OH^-}(\ K_W^*/K_2^*)$
$k_{W,f}$	1.40×10^{-3}	mol kg^{-1} s^{-1}	None
$k_{W,b}$	2.31×10^{-10}	kg mol^{-1} s^{-1}	$k_{W,f}/K_W^*$
A_4			$499002.24 \exp(4.2986 \times 10^{-4}S^2 + 5.75499 \times 10^{-5}S)$

A.2 Distribution current density

We have made a distribution of the current density based on the overpotential. The derivation is similar to the one done by Newman en Tobias [43]. As explained in 2.2.5, the significant overpotentials in our setup are the η_{ion} and η_{act}. As the overpotential, from one point to another point, is independent from the path it takes, the sum of $\eta_{\text{ion}}(x)$ and $\eta_{\text{act}}(x)$ is independent of x, so

$$\frac{\partial \eta_{\text{ion}}(x)}{\partial x} + \frac{\partial \eta_{\text{act}}(x)}{\partial x} = 0. \tag{53}$$

Where the x coordinate is where there electrochemical reaction happens. We combined **??** and eqs. (31) and (33) with eq. (53) to,

$$\frac{\partial}{\partial x}\frac{\int_0^x i_{\text{m}}(x)dx}{\kappa_{\text{eff}}} + \frac{\partial}{\partial x}(b\ln(-\frac{1}{a}\frac{\frac{\partial}{\partial x}i_{\text{m}}(x)}{i_0})) = 0, \tag{54}$$

rewritten as as a second order non linear equation,

$$i_{\text{m}}(x)b\frac{\partial}{\partial x}(i_{\text{m}}(x)) + \kappa_{\text{eff}}b\frac{\partial^2}{\partial x^2}(i_{\text{m}}(x)) = 0. \tag{55}$$

general solution,

$$i_{\text{m}}(x) = -\sqrt{2}\sqrt{c_1}\sqrt{\kappa_{\text{eff}}b}\tanh\frac{\sqrt{2}\sqrt{c_1}x + \sqrt{2}\sqrt{c_1}c_2}{2\sqrt{\kappa_{\text{eff}}b}} \tag{56}$$

We added boundary conditions

$$i_{\text{m}}(0) = i, \tag{57}$$

makes $c_1 \neq 0$ and

$$i_{\text{m}}(L) = 0. \tag{58}$$

therefore $c_2 = -L$, such that

$$i_{\text{m}}(x) = -\sqrt{2}\sqrt{c_1}\sqrt{\kappa_{\text{eff}}b}\tanh\frac{\sqrt{2}\sqrt{c_1}(x - L)}{2\sqrt{\kappa_{\text{eff}}b}} \tag{59}$$

Where we find c_1 by solving eq. (57) numerically. So the current distribution is depending on i, b, κ_{eff} and L. And interestingly it seems to be not depending by the particle diameter, even though κ_{eff}, is a function of the void fraction, which is influenced by the particle geometry. We plotted the current distribution for different current densities. Using eqs. (11) and (59), we can write,

$$i_{\text{in}}(x) = \frac{c_1}{a}\operatorname{sech}^2\frac{\sqrt{2}\sqrt{c_1}(x - L)}{2\sqrt{\kappa_{\text{eff}}b}}. \tag{60}$$

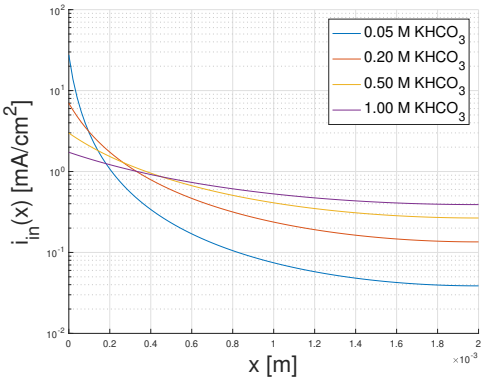

Figure 9: $i_{\text{in}}(x)$ at different $KHCO_3$ concentrations, which shows the great dependence of current distribution on the supporting electrolyte concentration.

This makes $i_{\text{in}}(x)$ linear dependent on d_{p}.

[]

A.3 Local conditions

The transport of the other components in the diffusion layer is a combination of diffusion and migration, as they have charge. As it is hard to measure the potential gradient in the diffusion boundary layer, the transference number [8],

$$t_j = \frac{|z_j u_j C_j}{\sum |z_i|, u_i C_i}, \tag{61}$$

helps to determine the flux of component j, where z_j, u_j, C_j, at the charge, the electrical mobility and the concentration of component j. We express the transport by migration as migration current,

$$i_{\text{m,j}} = \frac{n}{z_j} t_j i_{\text{in}}(x). \tag{62}$$

Subsequently the diffusion current of component j,

$$i_{\text{d,j}}(x) = i_j - i_{\text{m,j}}, \tag{63}$$

can be calculated, where i_j is the current of component j, which is equal to i_{in} when the component gets consumed or produced.

Table 5: Diffusion coefficients of components at 298.15 K and 1 bar, averages taken from multiple sources by Morrison at al. [41]. Mobility of ions taken from Bard en Faulkner [8]. [a] Taken from Parkhurst et al. [46].

Component	Diffusion coefficient $\times 10^{-9}\,\text{m}^2\,\text{s}^{-1}$	Mobility of ion $\times 10^{-7}\,\text{m}^2\,\text{s}^{-1}\,V^{-1}$
CO_2(aq)	2.0	
OH^-	5.3	2.05
HCO_3^-	0.92	0.461
CO_3^{-2}	1.2	[a] 1.435
H^+	[a] 1.96	3.625
K^+	[a] 9.31	0.7619

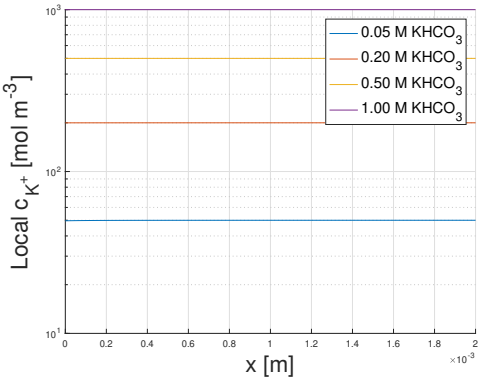

Figure 10: Plots the Local K^+ concentration over x, at 0.05, 0.20 and 1.00 M $KHCO_3$. The difference between the local and the bulk concentration can be neglected.

A.4 Instruments

Potentiostat electrodeposition

Model: BioLogics VSP-300[18]
Function: Power supply for the electrodeposition

Potentiostat CO_2R to CO

Model: bkprecision Model 9151
Function: Powersupply for the CO_2R to CO

Micro gas chromatograph (MGC)

Model: Varian CP4900
Function: Analyse the gas composition of the gas outlet stream

Hight performance liquid chromatograpy (HPLC)

Model: Agilent 1260 Infinity chromatograph
Function: Determine possible carbon products in the electrolyte

Scanning electron microscope (SEM)

Model: Jeol JSM-IT200 SEM
Function: Perform EDS measurements and obtain high magnification images of the electrode surfaces.

ICP

Model: ARCOS ICP-OES analyzer
Function: Check contaminations of ions in the solutions

A.5 CO_2 gas in output stream

The fraction of CO_2 gas in the output stream was measured to be between 40% and 65%, which can be seen in fig. 11. The CO_2 parts show a negative linear relationship with the flux of gaseous products, CO and H_2. Therefore, the flux of CO_2 is not proportional to the flux of gaseous reaction products.

The CO_2 desorbs, because of the decrease in partial pressures through the FTE. This decrease in pressure is due to pressure drops over the electrode and the appearance of other gases, CO and H_2, causing over-saturation. However, the desorption takes place rather slow [52]. The CO_2 desorption flux is also limited by the slow reaction kinetics of HCO_3^- to CO_2, which limits the amount of CO_2 that can be desorbed.

We expect that the main reason for the high concentration of CO_2 in the output stream is a long time in the gas-separation column. By lowering the time between reaction and separation, we can prevent high CO_2 concentrations in the output stream. Additionally, lowering the CO_2 concentration when purging, will also lower the over-saturation. Lower concentrations of CO_2 will not immediately decrease the cell performance by mass transport limitations, due to the higher diffusion rate in the FTE (see fig. 2). Thus, we believe that a CO-rich stream can easily be produced, without an energy-intensive separation step.

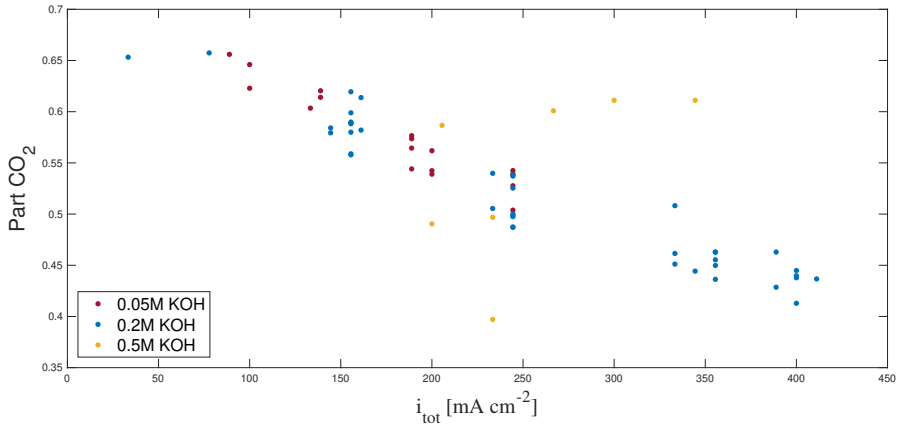

Figure 11: Total current vs. fraction of CO_2 in the gaseous products.

A.6 One-off CO_2R to CO experiment

The one-off results of performed without the BPM. The cell setup was identical to the setup used during deposition, but the electrolyte would flow through the GLS and bubble column like the other the earlier described CO_2R to CO experiment. Both the cathode and anode were operating in neutral pH. This gave enormous overpotential on the anode side. The overall cell potential was 21 V during this experiment. But we obtained the highest CO partial current density of 100 mA cm^{-2}, when having a FE of 55 %.

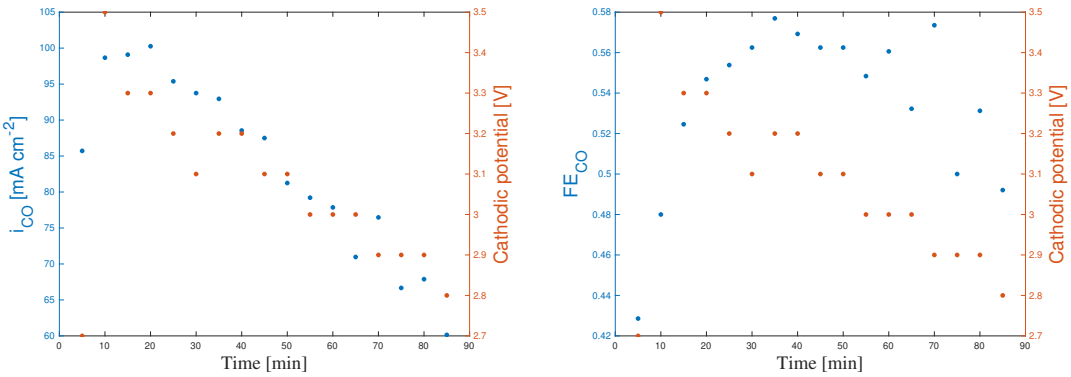

(a) (b)

Figure 12: Results of One-off CO_2R to CO experiment. The CO partial current density and Faradaic efficiency over time, in a 0.2 M $KHCO_3$ solution, with 21 V cell potential.

A.7 Additional SEM images

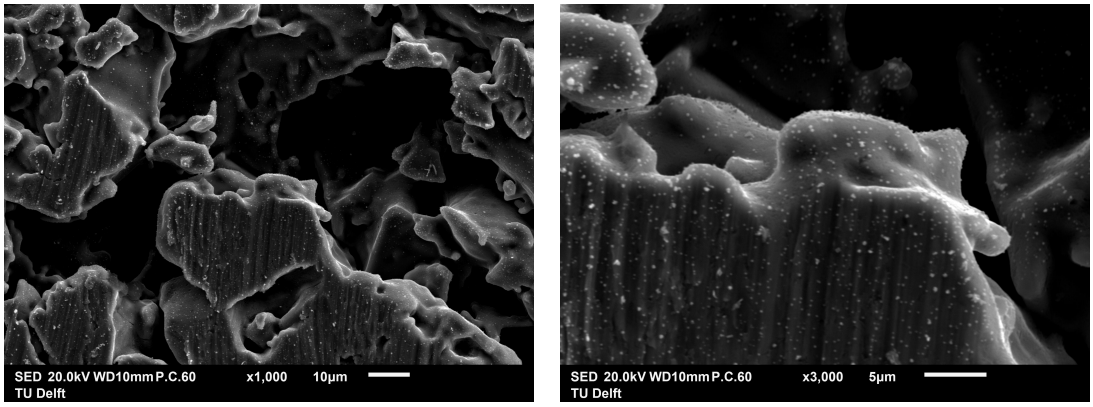

(a) (b)

Figure 13: SEM image of the front side after electrodeposition of Ag on the Ti 5 micron porous electrode at magnification of (a) 1000 times and (b) 3000 times, where the tiny white dots are the Ag particles.

A.8 Experimental setup

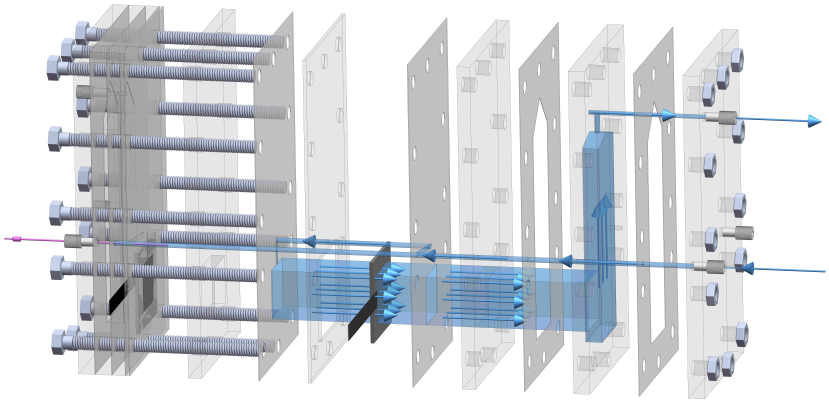

(a)

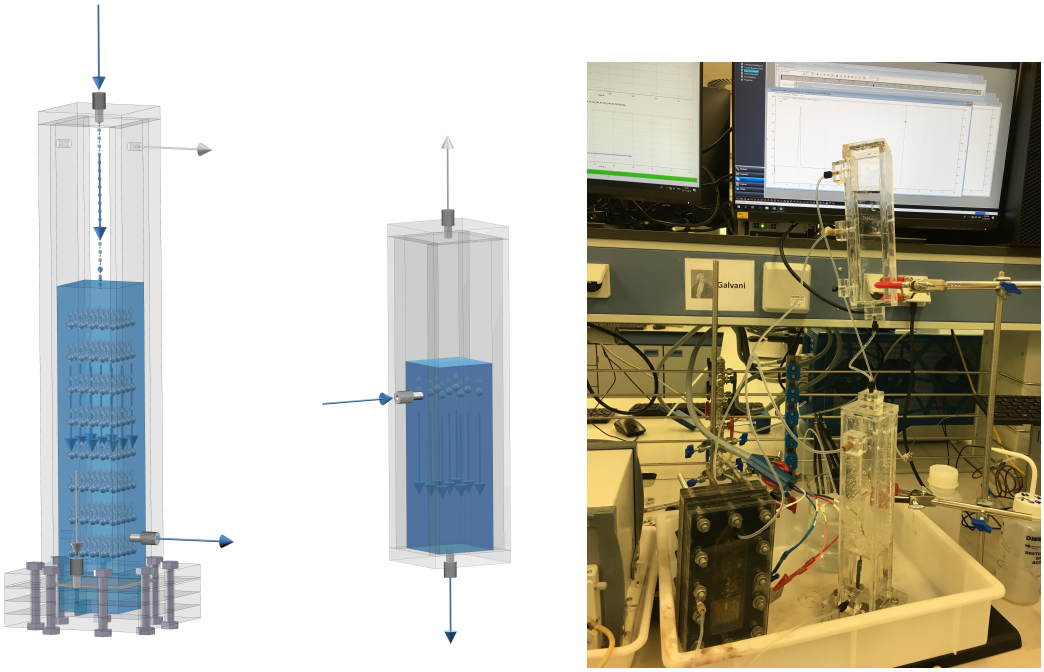

(b) (c) (d)

Figure 14: (a)A SolidWorks render of the experimental setup of the electrodeposition, in realistic proportions. Some colors differ from reality to distinguish the different components.(b) A SolidWorks render of the bubble column. White arrows showing the flow of bubbles up-words and blue arrows show the flow of electrolyte down-words. (c)A SolidWorks render of the GLS. White arrows showing the flow of bubbles up-words and blue arrows show the flow of electrolyte down-words. (c) The setup during experiments, left under the electrolyser, right under the bubble colums and right up de GLS.

References

[1] *Appendix 8: Electrical Conductivity of Selected Materials*. John Wiley Sons, Ltd, 2004, pp. 893–899. [Online]. Available: https://onlinelibrary.wiley.com/doi/abs/10.1002/0471473359.app8

[2] , "Silver / gold price ratio," https://www.indexmundi.com, Jan 2020.

[3] ——, "Titanium price," https://www.stindia.com, Jan 2020.

[4] D. Aaron, Q. Liu, Z. Tang, G. Grim, A. Papandrew, A. Turhan, T. Zawodzinski, and M. Mench, "Dramatic performance gains in vanadium redox flow batteries through modified cell architecture," *Journal of Power Sources*, vol. 206, pp. 450 – 453, 2012. [Online]. Available: http://www.sciencedirect.com/science/article/pii/S0378775311024451

[5] P. Alotto, M. Guarnieri, and F. Moro, "Redox flow batteries for the storage of renewable energy: A review," *Renewable and Sustainable Energy Reviews*, vol. 29, pp. 325 – 335, 2014. [Online]. Available: http://www.sciencedirect.com/science/article/pii/S1364032113005418

[6] B. G. Ateya, E. A. S. Arafat, and S. A. Kafafi, "Hydrodynamic effects on the efficiency of porous flow-through electrodes," *Journal of Applied Electrochemistry*, vol. 7, no. 2, pp. 107–112, Mar 1977. [Online]. Available: https://doi.org/10.1007/BF00611031

[7] Y. Bai and Q. Bai, "Chapter 18 - hydraulics," in *Subsea Pipelines and Risers*, Y. Bai and Q. Bai, Eds. Oxford: Elsevier Science Ltd, 2005, pp. 277 – 316. [Online]. Available: http://www.sciencedirect.com/science/article/pii/B9780080445663500208

[8] A. J. Bard and L. R. Faulkner, *Electrochemical methods: Fundamental and Applications*. Springer International, 2016.

[9] P. Bumroongsakulsawat and G. Kelsall, "Tinned graphite felt cathodes for scale-up of electrochemical reduction of aqueous co2," *Electrochimica Acta*, vol. 159, pp. 242 – 251, 2015. [Online]. Available: http://www.sciencedirect.com/science/article/pii/S0013468615002686

[10] R. Chattopadhyay, "1 - introduction: types of technical textile yarn," in *Technical Textile Yarns*, ser. Woodhead Publishing Series in Textiles, R. Alagirusamy and A. Das, Eds. Woodhead Publishing, 2010, pp. 3 – 55. [Online]. Available: http://www.sciencedirect.com/science/article/pii/B9781845695491500011

[11] H. Y. Cheh, "Electrodeposition of gold by pulsed current," *Journal of The Electrochemical Society*, vol. 118, no. 4, p. 551, 1971. [Online]. Available: https://doi.org/10.1149%2F1.2408110

[12] L. D. Chen, M. Urushihara, K. Chan, and J. K. Nørskov, "Electric field effects in electrochemical co2 reduction," *ACS Catalysis*, vol. 6, no. 10, pp. 7133–7139, 2016. [Online]. Available: https://doi.org/10.1021/acscatal.6b02299

[13] W. C. Chin, "Chapter 5 - more steady flow applications," in *Managed Pressure Drilling*, W. C. Chin, Ed. Boston: Gulf Professional Publishing, 2012, pp. 183 – 266. [Online]. Available: http://www.sciencedirect.com/science/article/pii/B9780123851246000058

[14] A. K. Coker, "4 - fluid flow," in *Ludwig's Applied Process Design for Chemical and Petrochemical Plants (Fourth Edition)*, fourth edition ed., A. K. Coker, Ed. Burlington: Gulf Professional Publishing, 2007, pp. 133 – 302. [Online]. Available: http://www.sciencedirect.com/science/article/pii/B9780750677660500117

[15] E. J. Dickinson, J. G. Limon-Petersen, and R. G. Compton, "The electroneutrality approximation in electrochemistry," *Journal of Solid State Electrochemistry*, vol. 15, no. 7-8, pp. 1335–1345, 2011. [Online]. Available: https://doi.org/10.1007/s10008-011-1323-x

[16] Dr. Pieter Tans and NOAA and Dr. Ralph Keeling, "Trends in atmospheric carbon dioxide," https://www.esrl.noaa, March 2020.

[17] European Commission, "Greenhouse gases," https://www.acs.org, 2020.

[18] ——, "Vsp-300," https://www.biologic.net, March 2020.

[19] M. Gillespie and R. Kriek, "Hydrogen production from a rectangular horizontal filter press divergent electrode-flow-through (deft) alkaline electrolysis stack," *Journal of Power Sources*, vol. 372, pp. 252 – 259, 2017. [Online]. Available: http://www.sciencedirect.com/science/article/pii/S0378775317314349

[20] Y. S. Ham, S. Choea, M. J. Kima, T. Limb, S.-K. Kimc, and J. J. Kima, "Electrodeposited ag catalysts for the electrochemical reduction of co2 to co," *Applied Catalysis B: Environmental*, vol. 208, pp. 35–43, 2017.

[21] J. Haverkort, "A theoretical analysis of the optimal electrode thickness and porosity," *Electrochimica Acta*, vol. 295, pp. 846 – 860, 2019. [Online]. Available: http://www.sciencedirect.com/science/article/pii/S0013468618323041

[22] W. Haynes, *CRC Handbook of Chemistry and Physics*, ser. CRC Handbook of Chemistry and Physics. CRC Press, 2011. [Online]. Available: https://books.google.nl/books?id=pYPRBQAAQBAJ

[23] Y. Hori, *Electrochemical CO2 Reduction on Metal Electrodes*. New York, NY: Springer New York, 2008, pp. 89–189. [Online]. Available: https://doi.org/10.1007/978-0-387-49489-0_3

[24] ——, *CO2 Reduction Using Electrochemical Approach*. Cham: Springer International Publishing, 2016, pp. 191–211. [Online]. Available: https://doi.org/10.1007/978-3-319-25400-5_12

[25] Y. Hori, H. Wakebe, T. Tsukamoto, and O. Koga, "Electrocatalytic process of co selectivity in electrochemical reduction of co2 at metal electrodes in aqueous media," *Electrochimica Acta*, vol. 39, no. 11, pp. 1833 – 1839, 1994. [Online]. Available: http://www.sciencedirect.com/science/article/pii/0013468694851727

[26] Y. Ida, S. Watase, T. Shinagawa, M. Watanabe, M. Chigane, M. Inaba, A. Tasaka, and M. Izaki, "Direct electrodeposition of 1.46 ev bandgap silver(i) oxide semiconductor films by electrogenerated acid," *Chemistry of Materials*, vol. 20, no. 4, pp. 1254–1256, 2008. [Online]. Available: https://doi.org/10.1021/cm702865r

[27] T. Kadyk, D. Bruce, and M. Eikerling, "How to enhance gas removal from porous electrodes?" *Scientific Reports*, vol. 6, no. 1, p. 38780, Dec 2016. [Online]. Available: https://doi.org/10.1038/srep38780

[28] J. V. Kenkel and A. J. Bard, "A dual working electrode coulometric flow cell," *Journal of Electroanalytical Chemistry and Interfacial Electrochemistry*, vol. 54, no. 1, pp. 47 – 54, 1974. [Online]. Available: http://www.sciencedirect.com/science/article/pii/S0022072874803797

[29] H. Khalifa, B. Ateya, and E. Arafat, "Electrochemical reduction of oxygen at a porous flow-through electrode," *Journal of Electroanalytical Chemistry and Interfacial Electrochemistry*, vol. 81, no. 2, pp. 301 – 307, 1977. [Online]. Available: http://www.sciencedirect.com/science/article/pii/S0022072877800260

[30] W. Knoche, "Chemical reactions of co2 in water," in *Biophysics and Physiology of Carbon Dioxide*, C. Bauer, G. Gros, and H. Bartels, Eds. Berlin, Heidelberg: Springer Berlin Heidelberg, 1980, pp. 3–11.

[31] S. Kumar and P. K. Muhuri, "A novel gdp prediction technique based on transfer learning using co2 emission dataset," *Applied Energy*, vol. 253, p. 113476, 2019. [Online]. Available: http://www.sciencedirect.com/science/article/pii/S030626191931150X

[32] M. König, J. Vaes, E. Klemm, and D. Pant, "Solvents and supporting electrolytes in the electrocatalytic reduction of co2," *iScience*, vol. 19, pp. 135 – 160, 2019. [Online]. Available: http://www.sciencedirect.com/science/article/pii/S2589004219302391

[33] S. Lamaison, D. Wakerley, J. Blanchard, D. Montero, G. Rousse, D. Mercier, P. Marcus, D. Taverna, D. Giaume, V. Mougel, and M. Fontecave, "High-current-density co2-to-co electroreduction on ag-alloyed zn dendrites at elevated pressure," *Joule*, vol. 4, no. 2, pp. 395 – 406, 2020. [Online]. Available: http://www.sciencedirect.com/science/article/pii/S2542435119305811

[34] S.-W. Lee, J.-K. Lee, K.-H. Lee, and J.-H. Lim, "Electrochemical reduction of co and h2 from carbon dioxide in aqua-solution," *Current Applied Physics*, vol. 10, no. 2, Supplement, pp. S51 – S54, 2010, the Proceeding of the International Renewable Energy Conference and Exhibition 2008 (RE2008). [Online]. Available: http://www.sciencedirect.com/science/article/pii/S1567173909005367

[35] S. Liu, H. Tao, L. Zeng, Q. Liu, Z. Xu, Q. Liu, and J.-L. Luo, "Shape-dependent electrocatalytic reduction of co2 to co on triangular silver nanoplates," *Journal of the American Chemical Society*, vol. 139, no. 6, pp. 2160–2163, 2017, pMID: 28150946. [Online]. Available: https://doi.org/10.1021/jacs.6b12103

[36] M. Ma, B. J. Trzeniewski, J. Xie, and W. A. Smith, "Selective and efficient reduction of carbon dioxide to carbon monoxide on oxide-derived nanostructured silver electrocatalysts," *Angewandte Chemie International Edition*, vol. 55, no. 33, pp. 9748–9752, 2016. [Online]. Available: https://onlinelibrary.wiley.com/doi/abs/10.1002/anie.201604654

[37] J. Macak, B. Gong, M. Hueppe, and P. Schmuki, "Filling of tio2 nanotubes by self-doping and electrodeposition," *Advanced Materials*, vol. 19, no. 19, pp. 3027–3031, 2007. [Online]. Available: https://onlinelibrary.wiley.com/doi/abs/10.1002/adma.200602549

[38] E. S. Menon, "Chapter 9 - series and parallel piping and power required," in *Pipeline Planning and Construction Field Manual*, E. S. Menon, Ed. Boston: Gulf Professional Publishing, 2011, pp. 177 – 204. [Online]. Available: http://www.sciencedirect.com/science/article/pii/B9780123838674000098

[39] F. J. Millero, T. B. Graham, F. Huang, H. Bustos-Serrano, and D. Pierrot, "Dissociation constants of carbonic acid in seawater as a function of salinity and temperature," *Marine Chemistry*, vol. 100, no. 1, pp. 80 – 94, 2006. [Online]. Available: http://www.sciencedirect.com/science/article/pii/S0304420305001921

[40] D. Moore, "The boundary layer on a spherical gas bubble," *Journal of Fluid Mechanics*, vol. 16, no. 2, pp. 161–176, 1963.

[41] A. R. T. Morrison, V. van Beusekom, M. Ramdin, L. J. P. van den Broeke, T. J. H. Vlugt, and W. de Jong, "Modeling the electrochemical conversion of carbon dioxide to formic acid or formate at elevated pressures," *Journal of The Electrochemical Society*, vol. 166, no. 4, pp. E77–E86, 2019. [Online]. Available: https://doi.org/10.1149%2F2.0121904jes

[42] M. Moura de Salles Pupo and R. Kortlever, "Electrolyte effects on the electrochemical reduction of co2," *ChemPhysChem*, vol. 20, no. 22, pp. 2926–2935, 2019. [Online]. Available: https://chemistry-europe.onlinelibrary.wiley.com/doi/abs/10.1002/cphc.201900680

[43] J. S. Newman and C. W. Tobias, "Theoretical analysis of current distribution in porous electrodes," *Journal of The Electrochemical Society*, vol. 109, no. 12, p. 1183, 1962. [Online]. Available: https://doi.org/10.1149%2F1.2425269

[44] K. Nielsch, F. Müller, A.-P. Li, and U. Gösele, "Uniform nickel deposition into ordered alumina pores by pulsed electrodeposition," *Advanced Materials*, vol. 12, no. 8, pp. 582–586, 2000. [Online]. Available: https://onlinelibrary.wiley.com/doi/abs/10.1002/%28SICI%291521-4095%28200004%2912%3A8%3C582%3A%3AAID-ADMA582%3E3.0.CO%3B2-3

[45] I. Nysing and I. Kramers, "Absorption of co2 in carbonate bicarbonate buffer solutions in a wetted wall column," *Chemical Engineering Science*, vol. 8, no. 1, pp. 81 – 89, 1958. [Online]. Available: http://www.sciencedirect.com/science/article/pii/0009250958800391

[46] D. Parkhurst and C. Appelo, "Phreeqc (version 3)a computer program for speciation, batch-reaction, one-dimensional transport, and inverse geochemical calculations," *Water Resources Div., Denver, CO*, 2011.

[47] B. A. Rosen, A. Salehi-Khojin, M. R. Thorson, W. Zhu, D. T. Whipple, P. J. A. Kenis, and R. I. Masel, "Ionic liquid–mediated selective conversion of co2 to co at low overpotentials," *Science*, vol. 334, no. 6056, pp. 643–644, 2011. [Online]. Available: https://science.sciencemag.org/content/334/6056/643

[48] K. Schulz, U. Riebesell, B. Rost, S. Thoms, and R. Zeebe, "Determination of the rate constants for the carbon dioxide to bicarbonate inter-conversion in ph-buffered seawater systems," *Marine Chemistry*, vol. 100, no. 1, pp. 53 – 65, 2006. [Online]. Available: http://www.sciencedirect.com/science/article/pii/S0304420305001684

[49] C. Shen, R. Wycisk, and P. N. Pintauro, "High performance electrospun bipolar membrane with a 3d junction," *Energy Environ. Sci.*, vol. 10, pp. 1435–1442, 2017. [Online]. Available: http://dx.doi.org/10.1039/C7EE00345E

[50] M. R. Singh, J. D. Goodpaster, A. Z. Weber, M. Head-Gordon, and A. T. Bell, "Mechanistic insights into electrochemical reduction of co2 over ag using density functional theory and transport models," *Proceedings of the National Academy of Sciences*, vol. 114, no. 42, pp. E8812–E8821, 2017. [Online]. Available: https://www.pnas.org/content/114/42/E8812

[51] M. R. Singh, Y. Kwon, Y. Lum, J. W. Ager, and A. T. Bell, "Hydrolysis of electrolyte cations enhances the electrochemical reduction of co2 over ag and cu," *Journal of the American Chemical Society*, vol. 138, no. 39, pp. 13 006–13 012, 2016, pMID: 27626299. [Online]. Available: https://doi.org/10.1021/jacs.6b07612

[52] S. Sircar and T. C. Golden, "Isothermal and isobaric desorption of carbon dioxide by purge," *Industrial & Engineering Chemistry Research*, vol. 34, no. 8, pp. 2881–2888, 1995. [Online]. Available: https://doi.org/10.1021/ie00047a042

[53] P. Stonehart, "Potentiodynamic determination of electrode kinetics for chemisorbed reactants: The ag/ag2o/oh- system," *Electrochimica Acta*, vol. 13, no. 8, pp. 1789 – 1803, 1968. [Online]. Available: http://www.sciencedirect.com/science/article/pii/0013468668800878

[54] N.-T. Suen, S.-F. Hung, Q. Quan, N. Zhang, Y.-J. Xu, and H. M. Chen, "Electrocatalysis for the oxygen evolution reaction: recent development and future perspectives," *Chem. Soc. Rev.*, vol. 46, pp. 337–365, 2017. [Online]. Available: http://dx.doi.org/10.1039/C6CS00328A

[55] Z. Sun, T. Ma, H. Tao, Q. Fan, and B. Han, "Fundamentals and challenges of electrochemical co2 reduction using two-dimensional materials," *Chem*, vol. 3, no. 4, pp. 560 – 587, 2017. [Online]. Available: http://www.sciencedirect.com/science/article/pii/S2451929417303996

[56] M. Tahir, L. Pan, F. Idrees, X. Zhang, L. Wang, J.-J. Zou, and Z. L. Wang, "Electrocatalytic oxygen evolution reaction for energy conversion and storage: A comprehensive review," *Nano Energy*, vol. 37, pp. 136 – 157, 2017. [Online]. Available: http://www.sciencedirect.com/science/article/pii/S221128551730294X

[57] T. Takashima, K. Hashimoto, and R. Nakamura, "Mechanisms of ph-dependent activity for water oxidation to molecular oxygen by mno2 electrocatalysts," *Journal of the American Chemical Society*, vol. 134, no. 3, pp. 1519–1527, 2012, pMID: 22206433. [Online]. Available: https://doi.org/10.1021/ja206511w

[58] M. R. Thorson, K. I. Siil, and P. J. A. Kenis, "Effect of cations on the electrochemical conversion of CO2to CO," *Journal of The Electrochemical Society*, vol. 160, no. 1, pp. F69–F74, nov 2012. [Online]. Available: https://doi.org/10.1149%2F2.052301jes

[59] S. Toan, W. O'Dell, C. K. Russell, S. Zhao, Q. Lai, H. Song, Y. Zhao, and M. Fan, "Thermodynamics of nahco3 decomposition during na2co3-based co2 capture," *Journal of Environmental Sciences*, vol. 78, pp. 74 – 80, 2019. [Online]. Available: http://www.sciencedirect.com/science/article/pii/S1001074218305485

[60] C. E. Tornow, M. R. Thorson, S. Ma, A. A. Gewirth, and P. J. A. Kenis, "Nitrogen-based catalysts for the electrochemical reduction of co2 to co," *Journal of the American Chemical Society*, vol. 134, no. 48, pp. 19 520–19 523, 2012, pMID: 23167268. [Online]. Available: https://doi.org/10.1021/ja308217w

[61] J. A. Trainham and J. Newman, "A comparison between flow-through and flow-by porous electrodes for redox energy storage," *Electrochimica Acta*, vol. 26, no. 4, pp. 455 – 469, 1981. [Online]. Available: http://www.sciencedirect.com/science/article/pii/0013468681870247

[62] B. J. Trzeniewski, O. Diaz-Morales, D. A. Vermaas, A. Longo, W. Bras, M. T. Koper, and W. A. Smith, "In situ observation of active oxygen species in fe-containing ni-based oxygen evolution catalysts: The effect of ph on electrochemical activity," *Journal of the American Chemical Society*, vol. 137, no. 48, pp. 15 112–15 121, 2015, pMID: 26544169. [Online]. Available: https://doi.org/10.1021/jacs.5b06814

[63] K. J. Vachaparambil and K. E. Einarsrud, "Numerical simulation of bubble growth in a supersaturated solution," *Applied Mathematical Modelling*, vol. 81, pp. 690 – 710, 2020. [Online]. Available: http://www.sciencedirect.com/science/article/pii/S0307904X20300172

[64] B. Vanrenterghem, B. Geboes, S. Bals, J. Ustarroz, A. Hubin, and T. Breugelmans, "Influence of the support material and the resulting particle distribution on the deposition of Ag nanoparticles for the electrocatalytic activity of benzyl bromide reduction," *Applied Catalysis B: Environmental*, vol. 218, p. 3542549, 2015.

[65] A. S. Varela, M. Kroschel, T. Reier, and P. Strasser, "Controlling the selectivity of co2 electroreduction on copper: The effect of the electrolyte concentration and the importance of the local ph," *Catalysis Today*, vol. 260, pp. 8 – 13, 2016, surface Analysis and Dynamics (SAND). [Online]. Available: http://www.sciencedirect.com/science/article/pii/S0920586115003594

[66] V. Vedharathinam, Z. Qi, C. Horwood, B. Bourcier, M. Stadermann, J. Biener, and M. Biener, "Using a 3D Porous Flow-Through Electrode Geometry for High-Rate Electrochemical Reduction of CO2 to CO in Ionic Liquid," *Applied Catalysis B: Environmental*, vol. 218, p. 3542549, 2015.

[67] D. A. Vermaas and W. A. Smith, "Synergistic electrochemical co2 reduction and water oxidation with a bipolar membrane," *ACS Energy Letters*, vol. 1, no. 6, pp. 1143–1148, 2016. [Online]. Available: https://doi.org/10.1021/acsenergylett.6b00557

[68] H. Wang, H. Yuan, S. Sae Hong, Y. Li, and Y. Cui, "Physical and chemical tuning of two-dimensional transition metal dichalcogenides," *Chem. Soc. Rev.*, vol. 44, pp. 2664–2680, 2015. [Online]. Available: http://dx.doi.org/10.1039/C4CS00287C

[69] W. Wang, Q. Zhao, J. Dong, and J. Li, "A novel silver oxides oxygen evolving catalyst for water splitting," *International Journal of Hydrogen Energy*, vol. 36, no. 13, pp. 7374 – 7380, 2011, hysydays. [Online]. Available: http://www.sciencedirect.com/science/article/pii/S0360319911006860

[70] R. Weiss, "Carbon dioxide in water and seawater: the solubility of a non-ideal gas," *Marine Chemistry*, vol. 2, no. 3, pp. 203 – 215, 1974. [Online]. Available: http://www.sciencedirect.com/science/article/pii/0304420374900152

[71] B. Xu and A. Yu, "Numerical simulation of the gas-solid flow in a fluidized bed by combining discrete particle method with computational fluid dynamics," *Chemical Engineering Science*, vol. 52, no. 16, pp. 2785 – 2809, 1997. [Online]. Available: http://www.sciencedirect.com/science/article/pii/S000925099700081X

[72] J. Yu, T. Zhang, and J. Qian, "4 - energy-efficiency standards of electrical motor products," in *Electrical Motor Products*, J. Yu, T. Zhang, and J. Qian, Eds. Woodhead Publishing, 2011, pp. 51 – 172. [Online]. Available: http://www.sciencedirect.com/science/article/pii/B9780857090775500049

[73] R. E. Zeebe and D. Wolf-Gladrow, "Chapter 1 equilibrium," in *CO2 in seawater: Equilibrium, kinetics, isotopes*, ser. Elsevier Oceanography Series. Elsevier, 2001, vol. 65, pp. 1 – 84. [Online]. Available: http://www.sciencedirect.com/science/article/pii/S0422989401800027

[74] Y. Zhang, Y. Xie, Y. Zhu, X. Lu, and X. Ji, "Energy consumption analysis for co2 separation from gas mixtures with liquid absorbents," *Energy Procedia*, vol. 61, pp. 2695 – 2698, 2014, international Conference on Applied Energy, ICAE2014. [Online]. Available: http://www.sciencedirect.com/science/article/pii/S1876610214033098

[75] Y. Zhang, G. Jacobs, D. E. Sparks, M. E. Dry, and B. H. Davis, "Co and co2 hydrogenation study on supported cobalt fischertropsch synthesis catalysts," *Catalysis Today*, vol. 71, no. 3, pp. 411 – 418, 2002, fischer-Tropsch synthesis on the eve of the XXI Century. [Online]. Available: http://www.sciencedirect.com/science/article/pii/S0920586101004680

[76] Q. Zheng, F. Xing, X. Li, G. Ning, and H. Zhang, "Flow field design and optimization based on the mass transport polarization regulation in a flow-through type vanadium flow battery," *Journal of Power Sources*, vol. 324, pp. 402 – 411, 2016. [Online]. Available: http://www.sciencedirect.com/science/article/pii/S0378775316306644

[77] L. Q. Zhou, C. Ling, H. Zhou, X. Wang, J. Liao, G. K. Reddy, L. Deng, T. C. Peck, R. Zhang, M. S. Whittingham, C. Wang, C.-W. Chu, Y. Yao, and H. Jia, "A high-performance oxygen evolution catalyst in neutral-ph for sunlight-driven co2 reduction," *Nature Communications*, vol. 10, no. 1, p. 4081, Sep 2019. [Online]. Available: https://doi.org/10.1038/s41467-019-12009-8